

Sensory Neuron Dysfunction in Orthotopic Mouse Models of Colon Cancer

Mihály Balogh

University of Groningen

Jixiang Zhang

The University of Texas MD Anderson Cancer Center

Caitlyn M. Gaffney

The University of Texas MD Anderson Cancer Center

Neha Kalakuntla

The University of Texas MD Anderson Cancer Center

Nicholas T. Nguyen

The University of Texas MD Anderson Cancer Center

Ronnie T. Trinh

The University of Texas MD Anderson Cancer Center

Clarissa Aguilar

The University of Texas MD Anderson Cancer Center

Hoang Vu Pham

The University of Texas MD Anderson Cancer Center

Bojana Milutinovic

The University of Texas MD Anderson Cancer Center

James M. Nichols

The University of Texas MD Anderson Cancer Center

Rajasekaran Mahalingam

The University of Texas MD Anderson Cancer Center

Andrew J. Shepherd (✉ ajshepherd@mdanderson.org)

The University of Texas MD Anderson Cancer Center

Research Article

Keywords: colon cancer, neuropathy, paraneoplastic neuropathy, DRG neuron, neuropathic pain

Posted Date: May 26th, 2022

DOI: <https://doi.org/10.21203/rs.3.rs-1662899/v1>

License: © ⓘ This work is licensed under a Creative Commons Attribution 4.0 International License. [Read Full License](#)

Version of Record: A version of this preprint was published at Journal of Neuroinflammation on August 12th, 2022. See the published version at <https://doi.org/10.1186/s12974-022-02566-z>.

Abstract

Reports of neurological sequelae related to colon cancer are largely restricted to rare instances of paraneoplastic syndromes, due to autoimmune reactions. Systemic inflammation associated with tumor development influences sensory neuron function in other disease models, though the extent to which this occurs in colorectal cancer is unknown. We induced orthotopic colorectal cancer via orthotopic injection of two colorectal cancer cell lines (MC38 and CT26) in two different mouse strains (C57BL/6 and Balb/c, respectively). Behavioral tests of pain sensitivity and activity did not detect significant alterations in sensory sensitivity or diminished well-being throughout tumor development. However, immunohistochemistry revealed widespread reductions in intra-epidermal nerve fiber density in the skin of tumor-bearing mice. Though loss of nerve fiber density was not associated with increased expression of cell injury markers in dorsal root ganglia, lumbar dorsal root ganglia neurons of tumor-bearing animals showed deficits in mitochondrial function. These neurons also had reduced cytosolic calcium levels in live-cell imaging and reduced spontaneous activity in multi-electrode array analysis. Bulk RNA sequencing of DRGs from tumor-bearing mice detected activation of gene expression pathways associated with elevated cytokine and chemokine signaling, including CXCL10. This is consistent with the detection of CXCL10 (and numerous other cytokines, chemokines and growth factors) in MC38 and CT26 cell-conditioned media, and the serum of tumor-bearing mice. Our study demonstrates in a pre-clinical setting that colon cancer is associated with latent sensory neuron dysfunction and implicates cytokine/chemokine signaling in this process. These findings may have implications for determining risk factors and treatment responsiveness related to neuropathy in colorectal cancer.

Introduction

Colorectal cancer, being the third-most common form of cancer, accounts for approximately 10% of cancer-related mortality [1]. In 2013, 771,000 people died of colorectal cancer globally [2]. Although colon cancer-related mortality and incidence has been decreasing slowly but steadily, hundreds of thousands of people in the USA alone are still affected yearly [3]. Therefore, new non-cytotoxic therapeutics are continuously developed (such as checkpoint inhibitors and other immunological modulators), but cytotoxic agents such as oxaliplatin are still a cornerstone of colon cancer treatment regimens [1, 4]. Current use of oxaliplatin-based regimens often comes with dose-limiting side effects and prolonged, debilitating neuropathy [4].

Most cancers are capable of producing cytokines, growth factors, chemotactic molecules, and proteases, hence influencing or inducing systemic inflammation and hypercoagulability [5, 6]. In addition to their roles in tumor growth, Some of these mediators may also play important roles in the development of neuropathic pain, e.g. complement 5 (C5), or the CXCR3 receptor, and its ligand CXCL10 [7, 8]. These modulators have been shown to be upregulated in experimental animals or patients suffering from colon cancer [9–13]. Taking these and other observations together, there is now clear evidence showing shared systemic processes involved in both the development of cancer and neuropathic pain [14].

Traditionally, paraneoplastic neuropathy (where clinical presentation of neuropathy symptoms is induced directly by cancer) is regarded as a rare complication [15, 16], and is typically characterized as a form of autoimmune or chronic inflammatory demyelinating polyneuropathy. What has not been explored as extensively is how widespread earlier symptoms of neuronal dysfunction may be. This is important because pre-existing neuropathy is a risk factor for subsequent development of neuropathic pain [17].

Despite these observations, the majority of pre-clinical data on neuropathic pain, including chemotherapy induced peripheral neuropathy (CIPN), are gained from studies where otherwise naïve animals are dosed with chemotherapy. Few studies have investigated neuronal dysfunction directly induced by tumor growth. Therefore, we set out to determine the extent to which preclinical models of colorectal cancer affect sensory neuron function, and by what means. We used two distinct mouse orthotopic colon cancer models: MC38 cells in C57BL/6 mice, and CT26 cells in Balb/c mice. After confirming engraftment, we investigated overall indicators of animal well-being (weight change, nestlet shredding assay), the development of typical neuropathic and tumor-related pain symptoms (mechanical sensitivity, cold allodynia, abdominal pain), and performed immunohistochemistry to investigate changes in intraepidermal nerve fiber (IENF) density, as one of the prominent symptoms of neuropathy. Neuronal dysfunction was also analyzed with the use of a mitochondrial function assay and immunohistochemistry on dorsal root ganglia from tumor-bearing and control animals. To further analyze neuronal function, intracellular Ca^{2+} levels and electrical activity of DRG neurons were compared by live-cell Ca^{2+} imaging and multi-electrode array analysis, respectively. Finally, utilizing cytokine protein arrays, and bulk RNA sequencing of dorsal root ganglia, we aimed to characterize tumor-induced changes in circulating factors and draw connections to transcriptional changes at the level of the DRG. Collectively, our data suggest that neuronal dysfunction could represent a latent but common complication of colorectal cancer, which could represent a potential risk factor for subsequent development of neuropathy, induced by chemotherapy or otherwise.

Methods

Generation and maintenance of luciferase-expressing MC38 and CT26 CRC cells

The MC38 colon adenocarcinoma cell line (C57BL/6 origin) was obtained from Kerablast, Boston, USA (catalog # ENH204-FP). Cells were maintained in 10 cm TC dishes at 37°C, 5% CO_2 . Cell culture media: Dulbecco's modified MEM (DMEM) with 10% fetal bovine serum (FBS), 2 mM glutamine, 0.1 mM nonessential amino acids, 1 mM sodium pyruvate, 10 mM HEPES, 1x penicillin/streptomycin. Firefly luciferase-expressing CT26 colon carcinoma cells (Balb/c origin) were obtained from Cellomics (catalog #: SC-1298) and maintained at 37°C and 5% CO_2 in RPMI-1640 Medium with 10% FBS and 1x penicillin/streptomycin.

In order to non-invasively measure tumor growth in C57BL/6 mice, we transduced MC38 cells with a lentivirus (catalog # FCT160; Kerablast, Boston, USA) containing the firefly luciferase (CMV) and neomycin resistance genes. Our procedure was based on the provider's protocol [18]. Briefly, cells were plated in six well cell culture plate in 2 ml growth medium. After cell growth reached ~ 80% confluence (48 hours), growth medium was aspirated and 2 ml transduction medium was added, containing 7.5 μl (approx. 7.5×10^5 CFU) of the virus. 24 h later, cells were selected for infection by adding 400 $\mu\text{g}/\text{ml}$ G418 to the growth medium [19]. This concentration was the minimum required to kill all uninfected MC38 control wells within 7 days. All clones were expanded and stocks cryopreserved. Firefly luciferase expression was verified *in vitro* with the addition of 150 $\mu\text{g}/\text{ml}$ luciferin (catalog #: LUCK-1G; Goldbio) immediately prior to reading luminescence with a Biotek Synergy plate reader.

Animals

All experiments and procedures involving the use of mice were approved by the University of Texas MD Anderson Cancer Center Animal Care and Use Committee at MD Anderson Cancer Center (Houston, TX, USA) in accordance with the National Institutes of Health's *Guide for the Care and Use of Laboratory Animals*. Every effort was made to minimize the number of mice used and their suffering. Animals were randomly assigned to individual experimental groups. Eight- to 14-week-old male mice (weighing 22–30 g) were used for each experiment. Male C57BL/6J (catalog #: 000664) and BALB/c (catalog #: 000651) mice were obtained from Jackson Laboratories and kept under 12:12 light:dark cycle (07:00 to 19:00 h) with access to food and water *ad libitum*. All mice were habituated to the housing environment for at least four days before experiments began.

Orthotopic colon cancer models: local MC38 and CT26 cell injections

Colon tumors were induced using minimally invasive transanal rectal injection, based on the methods of Donigan et. al [20]. Under isoflurane anesthesia (3% isoflurane in oxygen), 2×10^5 luciferase-expressing MC38 or 1×10^5 luciferase-expressing CT26 cells in 50 μ l growth medium were injected using a 0.3 ml (U30) insulin syringe, into the colorectal wall of C57BL/6 and BALB/c mice, respectively. Control mice were anesthetized and injected with 50 μ l vehicle (cell growth medium) in the same manner. No animals died or had to be euthanized as a result of tumor development during the 4-week experimental period.

IVIS Lumina in vivo bioluminescent imaging: non-invasive tumor growth measurements

Tumor growth was followed by *in vivo* non-invasive bioluminescent imaging (BLI) using an IVIS XR Lumina (PerkinElmer), as described previously, with slight modifications [21]. Mice were injected with D-luciferin (150 mg/kg, i.p. dissolved in sterile PBS). After 10 min, a 1 min exposure of the ventral aspect was captured. Luminescence was quantified within a circular ROI overlying the colorectal region for each animal and expressed as average radiance (p/s/cm²/sr) by the Living Image software (PerkinElmer). Tumor- and vehicle-injected mice were measured weekly. Animals not developing tumors (as indicated by elevated signal intensity of at least 500 p/s/cm²/sr on the second week after injection) were excluded from experiments and did not exhibit visible tumor development upon necropsy (less than 5% of mice, data not shown).

Behavioral assays

All behavioral assays were performed in the same room as which mice were housed. Before the start of any experiment, mice were habituated to the testing apparatus for 2 days prior to initiating testing. Experimenters were blinded to tumor/vehicle injection to the fullest extent possible, however, four weeks post-injection, swelling of the tumor mass in the perianal area was often readily apparent. All behavioral testing was carried out during the light cycle, between 08:00 and 12:00.

Nestlet Shredding Test

In order to assess the extent to which pain sensitivity could be obfuscated by debilitating effects of late-stage tumor growth, we employed a nestlet shredding assay [22], a well-described indicator of well-being and a physiological behavior in which healthy mice are motivated to engage [23, 24]. 24 h before testing began, nesting

material was removed from the home cages. The following day, mice were placed in individual cages and habituated for 1 h. After habituation, weighed nestlets (two-inch square) were placed into the cages. The percentage of the nestlet that was shredded and/or became detached from the original nestlet was calculated 3 h later.

Abdominal Sensitivity

An abdominal von Frey filament assay was performed to assess abdominal sensitivity changes induced by tumor growth [25]. Mice were placed in single-occupancy Plexiglas boxes, situated on a wire mesh platform. After 30 min of habituation, withdrawal behaviors were counted (withdrawal or licking of the abdomen as a result of stimulation, or whole-body withdrawal) in response to application of a 0.02 g von Frey filament to the lower abdomen. Each mouse was measured 5 times, with intervals of ~ 10 seconds. After a 1 min rest period this was repeated, resulting in a total of 10 filament applications per mouse. For each application, responses were scored as: 0 = no response; 1 = immediate slight attempt to escape or light licking or scratching of the stimulated site; 2 = intense withdrawal of the abdomen or jumping. The cumulative scores of the ten measurements are presented for each animal.

Behavioral test of sensorimotor function

The adhesive tape removal test of sensorimotor acuity was conducted as described previously [26]. Briefly, a 5 mm x 5 mm piece of electrical tape was applied to the center of the plantar surface of each hindpaw immediately before placement in single-occupancy Plexiglas boxes for observation. The time to initial contact with either piece of tape and the latency to removal of the tape from the hindpaw were recorded by blinded observers. Mice were habituated to restraint and to the test conditions 10- and 12-days post-tumor injection, before undergoing testing every 2 days for the next 10 days.

Hindpaw Mechanical and Cold Sensitivity

Before each experiment, animals were acclimated to the environment for at least 30 min on every testing day, and the day before the first testing. For the assessment of hindpaw mechanical allodynia, mice were placed in single-occupancy Plexiglas boxes, situated on a wire mesh platform. Von Frey filaments of increasing strength (0.04–2 g) were applied to the plantar surface of each hind paw until the filament was bent, starting with the 0.6 g filament in an up-down paradigm [27]. 50% paw withdrawal threshold values were calculated for each animal [27–29]. Measurements were performed before, and weekly after tumor cell injections for 4 weeks. Values are presented as the average percentage change compared to baseline. Cold sensitivity of mice was measured using powdered dry ice, based on [30]. Mice were habituated to single-occupancy Plexiglas boxes situated on a 6.35 mm-thick pane of glass. Powdered dry ice compacted into a 3ml syringe was applied to the glass directly underlying the plantar surface of each hind paw. Withdrawal latencies to this cooling stimulus were recorded in seconds using a stopwatch, and each paw was measured two times (with > 3 minutes between tests) and the mean latency calculated.

Immunohistochemistry

Dorsal root ganglia and 3 mm plantar punch biopsies of hind paws and fore paws were harvested after perfusion with 4% paraformaldehyde (PFA) in phosphate buffer (PB), pH 7.4, as described previously [31, 32]. At least 3 biological replicates/groups were measured from at least two different cohorts of mice for all tissues.

Plantar tissues were post-fixed in 4% PFA overnight before being transferred into 15% sucrose and 10% EDTA in PBS for 48 h for decalcification of bones, as described previously [33, 34]. After further incubation in 30% sucrose overnight, 40 µm lateral sections (skin to skin) were prepared with a Leica CM3050S cryostat and collected onto microscope slides. Immunohistochemistry was performed as previously described [31, 32]. After three 5-minute washes with 0.1 M PB, slides containing sections were blocked and permeabilized with 10% goat serum, and 0.3% Triton X-100 in 0.1 M PB for 1 h at 4°C. Sections were then incubated overnight at 4°C in primary antibodies diluted in blocking buffer (rabbit anti-PGP9.5: Thermo Fisher Scientific, catalog #38-1000; dilution: 1:500; rat anti-CD68, Bio-Rad, catalog #MCA1957GA; dilution: 1:300). The following day samples were washed 3 times in blocking buffer and then incubated with secondary antibody (1:1000 IgG-Alexa Fluor 488 goat anti-rabbit and goat anti-rat 568 antibody in blocking buffer and 1 µg/ml DAPI for 4 hours, protected from light at 4°C. Slides were then washed 3 times in 0.1M PB, mounted with ProLong Gold anti-fade reagent, coverslipped, sealed with nail polish and kept at -20°C until imaging with a Nikon Ti2 confocal microscope. Images were taken at 20 x magnification. Images are a composite of 10 focal planes in a 40 µm z-stack at 4 µm increments. Tissue samples from at least 3 mice/experimental group were imaged. 3–4 different sections were imaged from the same animal. Following image acquisition, intraepidermal nerve fiber (IENF) density was determined in the plantar skin as described previously [35–37] with the Nikon NIS-Elements Imaging Software and presented as number of IENFs/100 µm. CD68 signal intensity of the same tissue samples was determined in the hind paw skin by the application of ROIs from the edge of the plantar skin to 200 µm below the epidermis.

DRG samples were harvested and handled similarly to plantar punch tissue samples, as described previously [21, 31, 33]. Lumbar DRGs were harvested under a dissection microscope into 4% PFA, then placed into PBS containing 15% and 30% sucrose solutions in PBS, each overnight. 25 µm sections were stained using the same procedure as for plantar skin samples. For the stains performed using NF200, 1% BSA was added to the blocking buffer. After blocking for 1hr, sections were washed with PBS-Tween 20 (0.05%) and blocked with Goat F(ab) anti-mouse IgG H&L (Abcam, catalog#ab6668; dilution 1:50) in PBS for 1hr. The sections were rinsed again with PBS-Tween20 before the primary antibody was added in blocking buffer. The following primary antibodies were used for DRG immunofluorescence: rabbit anti-activating transcription factor 3 (ATF-3; Novus Biologicals, catalog #NBP1-85816; dilution: 1:300), rat anti-CD68 (Bio-Rad, catalog #MCA1957GA; dilution: 1:300), rabbit anti-CXCL10 (Thermo Fisher Scientific, catalog #701225; dilution 1:200), rabbit anti-CXCR3 (Thermo Fisher Scientific, catalog #PA5-23104; dilution 1:200), and mouse anti-NF200 (Sigma-Aldrich, catalog #N0142; dilution 1:200). Secondary antibodies: IgG-Alexa Fluor 594 goat anti-rabbit, IgG-Alexa Fluor 488 goat anti-rat (dilution: 1:1000), IgG-Alexa Fluor 488 goat anti-rabbit (dilution: 1:500), and IgG-Alexa Fluor 555 goat anti-mouse (dilution: 1:500). DAPI (1 µg/ml) was added together with the secondary antibodies.

Mitochondrial function assay

To determine tumor-related effects on neuronal mitochondrial bioenergetics, DRGs of tumor bearing and control animals were investigated by the XF^e24 Extracellular Flux Analyzer (Seahorse Bioscience), as described previously [35]. Immediately after collection of lumbar (L2-L5/6) DRG from tumor bearing and control mice into Ham's F10 media (Thermo Fisher Scientific, USA), connective tissue was removed, ganglia were enzymatically dissociated, and an enriched neuronal fraction was obtained [38]. Cells were plated into poly-DL-polyornithine (0.01%) / laminin (2 µg/mL)-coated XF24 plates (Seahorse Bioscience, Santa Clara, CA) in Ham's F10 medium containing N2 supplement without insulin at approximately 1,000 cells/well (Invitrogen). 24 h after plating, oxygen consumption rate (OCR) and the extracellular acidification rate (ECAR) was analyzed by the application

of an ATP synthase inhibitor (2 μM oligomycin), a protonophore that dissipates the proton gradient across the inner mitochondrial membrane (4 μM carbonilcyanide p-triflouromethoxyphenylhydrazone, FCCP), and the combination of a complex I and II inhibitor (2 μM rotenone and antimycin A, respectively). This enables determination of the portion of basal OCR coupled to ATP synthesis, the maximal respiratory capacity, and the amount of non-mitochondrial respiration [35, 39]. Dissociated DRGs were measured in an assay cycle of [3 min mixing, 2 min pause, 3 min measurement], repeated 3 times. Data were normalized to total protein levels, measured by BCA Protein Assay according to the manufacturer's instructions (Thermo Scientific; USA).

Live-cell calcium imaging

The live-cell calcium imaging (Ca^{2+} imaging) experiments were performed on cultured mouse DRG neurons as previously described [21, 40]. DRGs were collected from C57BL/6 mice as detailed in [41]. Isolated DRGs were digested with collagenase and pronase (2 mg/ml and 1mg/ml in DMEM, respectively). Before plating, the prepared cell suspension was centrifuged through a 1:1 28% and 12.5% Percoll density gradient (3900 rpm for 10 min), in order to remove non-cellular debris [42]. Thereafter, cells were plated onto poly-L-ornithine- and laminin-coated 12 mm circular glass coverslips and incubated in 1:1 TNB media supplemented with protein–lipid complex (Biochrom) and DMEM + 10% FBS at 37°C in 5% CO_2 for 1 to 2 days. Calcium imaging was conducted using Fura 2-AM, as described previously [21, 43]. Briefly, DRG neuron coverslips were incubated with the Ca^{2+} -sensitive dye Fura-2- AM (Invitrogen, 2 μM) at room temperature, for 20 min, dissolved in HEPES-buffered HBSS ('HH buffer') containing the following (in mM): 140 NaCl, 5 KCl, 1.3 CaCl_2 , 0.4 MgSO_4 , 0.5 MgCl_2 , 0.4 KH_2PO_4 , 0.6 NaHPO_4 , 3 NaHCO_3 , 10 glucose, and 10 HEPES adjusted to pH 7.4 with NaOH and adjusted to 310 mOsm with sucrose. Coverslips were then placed in an MS-512SP recording chamber (ALA scientific Instruments) on the stage of an inverted Nikon Ti2 microscope and continuously superfused for 5 min with HH buffer, fed through a valve-controlled gravity perfusion system with an approximate flow rate of 1 ml/min. The applied parameters during imaging: alternated Fura-2 excitation at 340 and 380 nm, 2 nm band-pass, 50 ms exposure) at 1 Hz using a Lambda LS Xenon lamp (Sutter Instruments, Novato, CA, USA) and a 10 x / NA 0.5 objective. Emitted fluorescence was collected at 510 nm (sCMOS pco.edge camera). The ratio of fluorescence (F340:F380) was calculated. The baseline recording of F340:F380 ratio without stimulus was performed to obtain an indication of resting intracellular calcium concentration ($[\text{Ca}^{2+}]_i$) under continuous superfusion of HH buffer at 37°C for 60 sec. Thereafter, neurons were stimulated by the application of 25 mM KCl solution in HH buffer, superfused for 15 sec, followed by superfusion with HH buffer for another 60 sec to wash out KCl. 50 mM KCl was applied at the end of the recording to identify all viable, excitable cells. Only neurons responding to 50 mM KCl were included in the data analysis. Imaging was analyzed with Nikon NIS Elements software.

Multi-electrode array recording of DRG neuron activity

DRGs were collected from C57BL/6 mice, digested and cleared of non-neuronal cells and debris as detailed in [41, 42]. Thereafter, cells were plated in 10 μl droplets (approximately 10^4 neurons per well) of 1:1 TNB media supplemented with protein–lipid complex (Biochrom) and DMEM + 10% FBS onto six wells of a 24-well CytoView MEA plate (Axion Biosystems). After 90 minutes, 365 μl of media was added to each well. Four hours after plating, a 15-minute recording of spontaneous activity each well was carried out on an Axion Maestro Edge at 37°C and 5% CO_2 . Continuous data were acquired simultaneously at 12.5 kHz per electrode (16 electrodes per well). Individual spikes were detected by filtered continuous data crossing of a 6 μV static threshold. Spike number and firing rate were calculated using Axion Neural Metrics Tool. Immediately after the four-hour

recording, 375 μ l of MC38 cell culture medium or MC38-conditioned media was added to each well. Conditioned media was collected from 2×10^6 MC38 cells grown overnight in a 10 cm tissue culture dish and centrifuged at 3900 rpm for 10 minutes to pellet any cellular debris. Subsequent 15-minute recordings were carried out at 8 hours and 20 hours *in vitro* (4 hours and 16 hours of exposure to MC38 media).

Bulk RNA sequencing from mouse DRGs

Lumbar DRG from control and MC38 tumor-bearing mice were collected after perfusion with PBS, and RNA was extracted using the RNeasy MinElute Cleanup Kit (Qiagen, Hilden, Germany), based on the manufacturer's protocol, as described previously [44]. The prepared samples were then shipped on dry ice and the bulk RNA sequencing (mRNA library preparation) was performed by Novogene (California, USA; California Clinical Laboratory License No: 05D2146243), after ensuring the samples met or exceeded the proper quality control criteria (Agilent 2100 RNA integrity number for all samples > 7). Raw reads in FASTQ format were analyzed using the FastQC tool for quality control [45]. The STAR package was used for the reference genome mapping with the mouse genome (mm10) [46]. The gene counts were estimated from uniquely mapped reads using the feature Counts program from the Subread tool [47]. Further, the gene counts were normalized and differentially expressed genes (p-value < 0.05) between the control and tumor-bearing mice were calculated using the DEseq2 program [48]. The pathway enrichment analysis was performed using the IPA tool with default parameters.

Proteome Profiler Antibody Arrays

Sera were isolated by centrifugation of blood samples collected by terminal cardiac puncture on control and tumor-bearing mice. Serum samples were analyzed semi-quantitatively using a mouse XL Cytokine Array Kit (R&D Systems, USA) to assess circulating tumor-associated inflammatory mediator levels 1 and 3 weeks after tumor injection. To investigate factors released directly by tumor cells, conditioned media samples were generated by collecting growth media after 24 h from 10 cm dishes at 80% confluence. Samples were incubated with spotted nitrocellulose membranes according to the manufacturer's instructions [49]. Protein concentration of samples was determined by a BCA assay prior to loading samples, to enable dilution of samples to normalize total protein content ($\sim 200 \mu$ g total protein). Membrane HRP luminescence intensities were visualized using an Amersham ImageQuant 800 biomolecular imager (Cytiva, USA), with an exposure time of 5 min and images were saved as high-resolution TIFF files. The registered intensity of each of the dots on the membranes was individually determined in duplicates by Image Studio software (version 5.2), and the fold increase was calculated compared to the average value of control samples. Negative control-, and reference spots were also analyzed in each experiment to validate the analyses. Three biological replicates were measured per condition.

Statistical analyses

All behavioral, histological and functional data are represented as mean \pm standard error of mean (SEM), and all analyses were performed using GraphPad Prism 8. Differences between multiple groups were analyzed by one- or two-way analysis of variance (ANOVA) with Sidak's multiple comparisons test, and $p < 0.05$ was considered statistically significant.

Results

Behavioral monitoring of the MC38 orthotopic colorectal cancer model.

Following colorectal injection of MC38 cells, C57BL/6 mice were monitored weekly for tumor growth using bioluminescent imaging (BLI; Fig. 1a). MC38-injected mice developed continuously increasing luciferase signal at the site of injection, indicating increasing tumor burden over time (Figs. 1b-c). In order to identify tumor-associated changes in pain sensitivity and/or general well-being, MC38-injected and vehicle-injected mice were assessed for their nestlet shredding behavior and abdominal and hindpaw mechanical sensitivity, along with hindpaw cold sensitivity and nestlet shredding behavior. We found no alterations in nestlet shredding behavior at 3 weeks post-MC38 injection, suggesting there is no debilitating pain sensitivity or disruption to spontaneous behavior at this timepoint (Fig. 2a). This observation was also underlined by no significant differences in the increase in animal weights compared to controls throughout the testing period (Fig. 2b). MC38 tumor burden also did not elevate abdominal mechanical sensitivity in the first 3 weeks. However, 4 weeks after injection, MC38 tumor-bearing mice showed a strong trend toward increased sensitivity compared to vehicle-injected controls (Fig. 2c). Collectively, these data suggest MC38 tumor burden does not cause overt debilitation or augment visceral pain sensitivity during the four-week experimental period. We also did not detect any statistically significant changes in hindpaw von Frey withdrawal thresholds (Fig. 2d), latency to detect/remove adhesive tape (Fig. 2e), or withdrawal latencies in response to cooling (Fig. 2f), suggesting that no obvious shifts in tactile or cold sensitivity are induced by MC38 tumor growth.

MC38 colon tumor induces IENF loss

Having seen no clear evidence of debilitation or sensorimotor dysfunction in MC38-injected mice, we next assessed MC38-induced changes to IENF density in the plantar skin, a prominent symptoms of peripheral neuronal damage [37, 39]. Plantar punch biopsies of hindpaws from tumor-bearing and control animals were analyzed by immunohistochemistry weekly after MC38 cell injection. We found no change in hindpaw IENF density (nerve endings/ 100 μ m of epidermis) in the first two weeks post-injection (Fig. 3a). However, at 3 and 4 weeks, there was a significant decrease in IENF density in tumor-bearing animals compared to vehicle-injected controls (Fig. 3b). To investigate whether this phenomenon was systemic, or restricted only to sensory innervation that overlaps with the thoracolumbar (T10-L1) and lumbosacral (L6-S1) innervation of the colon/rectum [50], we also analyzed forepaw skin, which is innervated by levels C6-T2, and as such does not innervate the colon/rectum [51]. We also found a significant decrease in IENF density in forepaw skin at the third week of MC38 tumor development (Fig. 3c-d), indicating that reduced IENF density is not confined to those ganglia that also provide sensory innervation to the colon. This significant alteration suggested that peripheral nerve endings experience injury/damage in MC38-injected mice, despite finding no significant changes in mouse well-being or pain-related behaviors. Since prior studies of nerve injury have reported increased macrophage density in the skin [21], we determined macrophage density in skin biopsies three weeks after MC38 injection, using the macrophage marker CD68. We found no alterations in CD68 density in the hind paw skin of tumor bearing mice (Fig. 3e-f), indicating that the IENF loss associated with MC38 injection does not elevate skin macrophage density.

MC38 tumor does not change neuronal damage-, or macrophage marker intensity in mouse DRG

Since MC38 tumor growth was associated with systemic reductions in IENF density, we investigated well-established indicators of neuronal damage at the level of the DRG: elevated macrophage density and increased expression of ATF-3 [52–54]. We did not observe any significant changes in lumbar DRG CD68 density or ATF-3 expression in samples from tumor bearing vs control mice (Fig. 4a-c). In contrast, repeat dosing with oxaliplatin (cumulative dose: 12 mg/kg i.p.) as a positive control did significantly elevate ATF-3 expression (Fig. 4b). This suggests that MC38 tumor-induced IENF loss is not associated with conventional markers of neuronal damage in the DRG.

MC38 colon tumor induces deficits in DRG mitochondrial function, calcium flux and electrical activity

A well-described mechanism of neuropathic pain is mitochondrial dysfunction in sensory neurons [55]. Therefore, we tested whether MC38 tumor growth was associated with mitochondrial dysfunction in mouse DRGs. Despite not detecting elevated ATF-3 expression or CD68⁺ macrophage density, MC38 tumor development led to significant mitochondrial dysfunction in the DRGs of tumor bearing animals, by the third week after MC38 injection (Fig. 5a-c). This is indicated by significant changes in both the oxygen consumption rate (OCR; Fig. 5a) and the extracellular acidification rate (ECAR; Fig. 5b), along with reduced ATP production and spare respiratory capacity (Fig. 5c). Importantly, these effects were observed on DRGs pooled from every level between C4 and L5, again suggesting this phenomenon may not be restricted to those DRG neurons innervating the colon

Since mitochondrial function is a major contributor to calcium dynamics in DRG neurons [56], we next performed live-cell calcium imaging of DRGs from control and MC38 tumor-bearing mice. (Fig. 5d-e). DRG neurons from MC38 tumor-bearing mice showed a small but significant decrease in baseline 340:380 nm Fura-2 ratio (Fig. 5d), indicating decreased resting $[Ca^{2+}]_i$ levels. Lumbar and non-lumbar DRG neurons were cultured and tested separately (data not shown), but, since no differences were observed, the data were pooled. Despite this decrease in baseline $[Ca^{2+}]_i$, the response to a depolarizing stimulus (25 mM KCl) [43] did not show any difference in response amplitude (Fig. 5e). Finally, we wanted to establish whether exposure to MC38-derived factors could be altering DRG neuron activity. Naïve C57BL/6 DRG neurons were dissociated and cultured on multi-electrode array plates. Four hours after plating, 50% of growth media was exchanged for fresh MC38 media ('control media') or media in which MC38 cells had been grown for 48 h ('MC38 conditioned media'). At 20 h *in vitro*, DRG neurons exposed to MC38 conditioned media displayed a significantly lower spontaneous firing rate (Fig. 5f). Collectively, this suggests that MC38-derived factors can influence DRG mitochondrial function and calcium homeostasis, which may underlie the reduced activity of cultured DRG neurons.

MC38 tumor growth is associated with inflammatory mediator production

In order to assess the secreted factors that could be driving MC38-induced DRG neuron dysfunction, we analyzed MC38 secretory output using Proteome Profiler assays (Mouse XL Cytokine Array Kit; R&D Systems [49]). Culture media in which MC38 cells were grown (2×10^6 cells, 48 h) was compared with uncultured media. Factors showing ≥ 1.2 -fold increase compared to control are depicted in Fig. 6a. Abundant secretion of chemokines (CXCL1, CCL2, CX3CL1, CCL5, CXCL10, CCL11) and growth factors (GDF-15, VEGF, M-CSF, FGF-21, amphiregulin) was detected in MC38-conditioned media. We also collected serum from MC38 tumor-bearing mice and vehicle injected controls, 1 week and 3 weeks after MC38 injection. At week 1, elevated levels of cytokines (IL-1 α , IL-6),

chemokines (CXCL2, CCL2, CCL3/4, CCL20) and growth factors (EGF, FGF acidic, PDGF-BB) were detected (Fig. 6b). 3 weeks after MC38 injection, the following mediators were shown to be increased by more than a 1.2-fold (in decreasing order): GM-CSF, G-CSF, GDF-15, HGF, Osteoprotegerin, IL-23, Proliferin, Pentraxin-2, CCL6, CXCL10, BAFF, Angiopoietin-2, Osteopontin, Lipocalin-2, CXCL1, IL-28A, Gas6, Proprotein Convertase 9, Serpin E1, CXCL16, P-Selectin (Fig. 6c). IFN- γ , IGFBP-1, IL-23, Endoglin and Serpin E1 were elevated in tumor-bearing serum at both timepoints (Fig. 6d). Altogether, seven factors were detected both in MC38-conditioned media and MC38 tumor-bearing serum: CCL2, GDF-15, Proliferin, CXCL10, Osteopontin, PCSK9 and Serpin E1. In agreement with our data, the chemokines shown to be increased here were also found to be elevated in different previous studies investigating cancer or neuropathic pain. Given their extensive role in the development of different neuropathies (including CIPN [57]), it is plausible that some of these factors play a significant part in the neuropathy observed here as well.

MC38 tumors induce transcriptional changes in the DRG

In order to better understand the signaling events and gene expression changes that MC38 tumors may be inducing to elicit functional changes in neuronal physiology, we subjected lumbar DRGs from MC38 cancer cell injected mice and control to bulk RNA-sequencing (Fig. 7). 134 differentially expressed genes were identified, 39 of which were significantly upregulated (Fig. 7a and **Additional Table 1**). Functional and disease enrichment analysis on up-regulated genes from the tumor bearing mice showed cancer as a top enrichment (number of genes: 23, see **Additional Fig. 1a-b**). Consistent with the elevated levels of multiple cytokines and chemokines in tumor-bearing serum, the pathway analysis showed the most robust increase in the 'Role of hypercytokinemia/hyperchemokinememia in the Pathogenesis of Influenza' pathway, along with numerous other inflammation-related pathways (Fig. 7b). Several pathways related to thrombosis / coagulation are also consistent with the hypercoagulable state attributed to colon cancer [58]. Collectively, these data indicate that the tumor induces transcriptional changes due to systemic inflammation. Of particular note is the significant upregulation of CXCL10 expression (Log₂ fold increase: 0.843, p = 0.012). This increased expression in bulk RNA is likely derived from DRG neuron somata, as they are the chief CXCL10-immunoreactive cell type in immunohistochemistry (Fig. 7c). It is notable that the proteome profile data also identified elevated expression of this chemokine in MC38 tumor-bearing mouse serum.

CT26 orthotopic colon cancer model in BALB/c mice

We next set out to determine if the disruption of DRG neuron function seen in MC38 tumor-bearing mice would generalize to other mouse strains and cancer cell lines. Similar to the MC38 model, we carried out orthotopic injection of luciferase-expressing CT26 cells into Balb/c mice, followed *in vivo* by bioluminescence measurements (Fig. 8a). We found a significant increase in bioluminescence signal at the 1st week after cell injection, which continuously further elevated during the 3-week time period (Fig. 8b), indicating the development of colon cancer. Again, similarly to the MC38 model, we found no significant differences in animal weight (Fig. 8c). Mechanical sensitivity of mice was assessed one, two and three weeks post-tumor injection. Similar to the MC38 model, we found no significant change in hindpaw mechanical sensitivity throughout the 3-week time period (Fig. 8d). Crucially, 3 weeks after CT26 tumor cell injection, a significant decrease in the IENF density of samples from the tumor group was observed (Fig. 8e-f), without any change in macrophage density (Fig. 8g-h), mirroring the sensory neuron dysfunction seen in C57BL/6 mice with MC38 cells. This IENF loss was again accompanied by mitochondrial dysfunction in the DRGs of tumor bearing animals, as indicated by significant changes in both OCR and ECAR (Fig. 9a-c).

CT26 tumor-induced inflammatory changes

To investigate the tumor induced inflammatory alterations in BALB/c mice, a cytokine array experiment was performed on mouse plasma samples 3 weeks after CT26 tumor cell injection. An additional table shows all measured cytokines [see **Additional tables 2–3**]. Similar to the MC38 model, we found robust alterations in secreted factor output in CT26-conditioned media (Fig. 10a). The following mediators showed at least a 1.2-fold signal increase compared to un-conditioned media samples: cytokines (IL-1 α / β , IL-2, IL-11, IL-12 p40, IL-27 p28, LIF) chemokines (CXCL1, CXCL2, CCL2, CX3CL1, CCL5, CCL17, CCL19, CXCL10, LIX) and growth factors (Osteoprotegerin, IGFBP-1/3/6, M-CSF, VEGF) predominate (Fig. 10a). In serum of CT26 tumor-bearing mice, there was extensive overlap with the factors detected in CT26-conditioned media: following mediators identified in conditioned media showed at least a 1.2-fold increase in CT26 tumor-bearing mice: IL-1 α , IL-2, IL-13, CCL2/5/19, LIX, CX3CL1, CXCL1/2/10 and CCL19 (Fig. 10b).

Across serum, conditioned media and both tumor types, four factors are consistently detected: CCL2, CXCL1, CXCL10 and Serpin E1. Collectively, these data indicate that similar proinflammatory pathways across two colorectal cancer models are associated with subclinical mitochondrial dysfunction and IENF loss in sensory neurons.

Discussion

With improved treatment of colorectal cancer comes the potential for long-term side effects in survivors, a population that is set to continue growing for the foreseeable future [59]. Although clinical data highlight peripheral neuropathy as a major side-effect in cancer survivors [60] and the fact that the pro-inflammatory milieu generated by tumors can affect neuronal function [4, 6], the extent to which colorectal cancer is directly responsible for neuropathy symptoms remains under-explored. Therefore, we set out to determine whether inflammation related to colorectal cancer was capable of inducing neuronal dysfunction/damage. Our study demonstrates colon tumor-initiated neuronal damage in a preclinical setting, by the application of orthotopic colon cancer models in two different mouse strains. Local (trans-anal) inoculation of both MC38 and CT26 cancer cells led to continuous tumor development without overt changes in measures of overall activity, shifts in pain sensitivity or cachexia (Fig. 2, Fig. 8c-d). Only four weeks post-tumor injection did tumor-bearing mice begin to develop a trend toward abdominal hypersensitivity and reduced/stalled weight gain (Figs. 2b, 8c). The most typical symptoms of neuropathic pain, cold and mechanical hypersensitivity were also investigated throughout the 4 week time period [61]. Based on our findings, tumor development did not lead to significant cold or mechanical hypersensitivity in this time period (Figs. 2d-f, Fig. 9d).

Despite the lack of behavioral symptoms consistent with neuropathy, we assessed IENF density in paw skin by immunohistochemistry, as a decrease in IENF density is among the most typical indicators of peripheral neuropathy [62, 63]. Damage of peripheral neurons was detected as decreased IENF density in hindpaw skin of tumor-bearing mice three weeks after cancer cell injection, which persisted into the fourth week. Since the dermatomes of the forepaw are innervated by ganglia outside of the thoracolumbar innervation of the lower GI tract [50], a similar reduction in forepaw skin IENF density suggested to us that tumor growth systemically reduces IENF density, rather than injuring DRG neurons that innervate both the colorectum and epidermis. This association between tumor growth and IENF loss is supported by the observation that colon cancer patients commonly show symptoms of peripheral neuronal damage when tested (IENF density loss; minor sensory

deficits in the extremities), despite not presenting with overt symptoms of pain or sensory loss [60, 63]. That said, it is important to underline that there is not always a direct association of IENF loss with neuropathic symptoms, and further work is needed to understand the degree to which tumor-induced neuropathy modifies lifetime risk of neuropathic pain [63, 64].

We then determined the extent to which indicators of nerve injury were present at the level of the DRG, namely macrophage infiltration [52] and ATF3 expression [65]. Consistent with the lack of alteration in pain behaviors, we did not detect increased macrophage density or ATF-3 expression in the DRG, both of which are reported features of overt neuropathic pain hypersensitivity seen following induction of CIPN or traumatic nerve injury. Finally, one of the main factors underlying neuropathy and neuropathic pain is mitochondrial dysfunction [17, 55, 66]. Therefore, we analyzed the mitochondrial function of lumbar DRGs from tumor-bearing mice, 3 weeks after tumor induction (first timepoint of IENF loss). The Seahorse assay revealed substantial mitochondrial dysfunction indicated by both OCR and ECAR (Fig. 5a-c, Fig. 9). Deficits of this magnitude (approximately 30% reduction in OCR) are less severe than those seen in models of cisplatin-induced CIPN (typically 50–60% reduction in OCR), changes that are associated with significant pain hypersensitivity and IENF loss [28]. This suggests that the relationship between mitochondrial dysfunction and pain hypersensitivity may be non-linear, that the onset of mitochondrial dysfunction occurs prior to the development of pain hypersensitivity, or that mitochondrial dysfunction induced by tumor growth is uncoupled from pain hypersensitivity. At this point, we cannot rule out mitochondrial dysfunction/reduced ATP production in tissues outside the DRG. Indeed, such effects have been reported in the skeletal muscle of patients with cancer [67, 68], though the energy demands and post-mitotic nature of neurons makes them particularly vulnerable [69, 70]. As such, our data are consistent with observations that energy availability and metabolic derangement are common features of cancer and cancer-related fatigue [71–73].

To further address the nature of the tumor-induced neuronal dysfunction, live-cell *in vivo* calcium imaging was performed on DRG neurons. Our analysis revealed reduced intracellular Ca^{2+} levels ($[Ca^{2+}]_i$) in DRG neurons from tumor-bearing mice. Though this can appear counterintuitive when compared with chronic pain states which tend to show hyperexcitability [74], this finding is consistent with prior reports showing low $[Ca^{2+}]_i$ after neuronal damage [75–79]. For example, Andreas Fuchs and co-workers showed that spinal nerve ligation decreased resting $[Ca^{2+}]_i$ levels in rat DRGs [77]. Reduced neuronal $[Ca^{2+}]_i$ is known to precipitate cell loss, a feature in different forms of neuropathy [77, 80]. However, it is unclear as yet if reduced $[Ca^{2+}]_i$ is directly tied to neuropathy and IENF loss, or the extent to which this is due to a systemic hypocalcemic state, as has been reported for hematological and colorectal cancers [81].

Mitochondria play a prominent role in neuronal Ca^{2+} signaling [82], and abnormal mitochondrial function can lead to axonal degeneration as well as disturbances in Ca^{2+} homeostasis, which can manifest in low $[Ca^{2+}]_i$ levels and neuronal damage [83]. The specific contribution of plasma membrane and organelle Ca^{2+} pumps, such as the sarco-endoplasmic reticulum Ca^{2+} -ATPase (SERCA), should be investigated, since they may contribute to reduced $[Ca^{2+}]_i$ levels, mitochondrial dysfunction and/or ER stress [78]). In summary, colon tumor growth leads to asymptomatic, but prominent neuronal dysfunction, which may have clinical implications for any future neurological insult incurred as a side-effect of cancer treatment.

In search of circulating factors that could underlie the systemic effects on sensory neurons, cytokine arrays of plasma samples from tumor bearing and control mice revealed robust systemic inflammatory changes (Figs. 6, 10). Interferon- γ was notable for its detection both 1 week and 3 weeks after tumor injection. Notably, several chemokines (CCL2, CXCL1, CXCL2, CXCL10) were shown to be increased in plasma samples as well as to be released by both investigated cancer cell lines (MC38, CT26), many of which are classed as 'interferon-stimulated genes' [84], an assertion borne out by our DRG RNA sequencing data (Fig. 7). Prior studies have found increases in chemokine expression in tissues from colorectal cancer patients that are associated with disease progression [85, 86]. The pathway enrichment analysis showed the most significant increase in the 'Role of Hypercytokinemia/hyperchemokinememia in the Pathogenesis of Influenza' pathway, further underlining the likely significant role of chemokines in the observed alterations.

In addition to pro-inflammatory signaling, the other main pathways highlighted by the RNAseq data relate to hemostasis/hypercoagulability (e.g. 'role of tissue factor in cancer,' 'intrinsic/extrinsic prothrombin activation pathway,' 'coagulation system'). Colorectal cancer is often associated with hypercoagulability in patients, to the extent it substantially increases the risk of thrombosis [58]. It is plausible that impaired endoneurial blood flow results from such clotting events, contributing to mitochondrial dysfunction and neuropathy, though this needs to be addressed experimentally.

There is a growing body of literature showing the multifaceted roles of chemokines in neuropathic pain development. Literature data indicates that the expression of chemokines and their receptors, such as CCL2/CCR2, CXCL1/CXCR2, (among others) are altered in CIPN [57]. CXCL2 has been also shown promote neuropathic pain in a recent study on a rat model of trigeminal neuropathic pain [87]. In addition, a large number of studies suggests the key role of CXCL10/CXCR3 signaling in the pathophysiology of different neuropathies [88–90]. Our results from the bulk RNA sequencing on DRGs from MC38 tumor bearing mice also revealed a significant increase in the expression of CXCL10 (Fig. 7). The extent to which the inflammatory signatures at the level of the DRG are a cause or consequence of DRG mitochondrial dysfunction remains to be established. NLRP3 inflammasome activation and subsequent production of inflammatory mediators could be downstream of ROS production from dysfunctional mitochondria [91], or inflammatory mediator signals originating from the circulation could be responsible for inducing DRG mitochondrial dysfunction.

It is well-established that pre-existing neuropathy of various etiologies is a risk factor for subsequent development of neuropathic pain [17]. In this context, tumor-induced neuropathy may have major implications for CIPN. Oxaliplatin treatment is still a cornerstone of colon cancer therapy and is well described to cause CIPN (in 90% of patients). However, a subset of patients (about 40%) develop chronic, intractable CIPN symptoms (such as mechanical allodynia or cold hypersensitivity) [17]. The risk factors leading to this detrimental chronic condition are still not understood. However, based on our observations, tumor induced inflammation may represent a crucial risk factor in chronic CIPN development, which should be further investigated in the future.

In order to further confirm our observations on peripheral neuronal dysfunction, and to increase the generalizability of our findings, we employed the same model on a different genetic background, engrafting CT26 cells into BALB/c mice. Without significant alterations in behavior, the CT26 model showed a similar decrease in IENF density, as well as indicators of mitochondrial dysfunction in DRG neurons (at the same time point as in the MC38 model – 3 weeks after engraftment, Fig. 8). The proteome profiler arrays of serum 3 weeks

after engraftment depicted a similarly robust systemic inflammation, with substantial overlap with the MC38 model (i.e. chemokines), as described above (Fig. 10).

Taken together, our study depicts colon cancer-induced peripheral neurological dysfunction in a preclinical setting (by the application of orthotopic colon cancer models), as indicated by: IENF density decrease in the skin of fore and hind paws; mitochondrial dysfunction of lumbar DRG neurons and reduced resting $[Ca^{2+}]_i$ in DRG neurons. The observed neurological dysfunction was not accompanied by behavioral changes, or any significant changes in the investigated parameters of animal well-being. Additionally, tumor development led to robust systemic inflammatory changes. The chemokines, CCL2, CXCL1, CXCL2, CXCL10 were shown to be increased across both tumor models. CXCL10 expression was also increased in the DRGs of MC38-inoculated mice.

It remains to be seen if the pro-inflammatory and hypercoagulable state associated with other cancer types elicits similar neuronal dysfunction, but subclinical peripheral neuropathy is also known to occur in patients with lung cancer or multiple myeloma [15, 92], suggesting this phenomenon may extend beyond colorectal cancer. Our observations indicate that the tumor induced systemic changes include peripheral neuronal dysfunction, without any pharmacological or other intervention. The increased mediators might be crucial in the induction of chronic, intractable CIPN, developing in a subset of colon cancer patients. This and the exact mechanism by which colon tumor induces systemic, peripheral neuronal dysfunction in mice warrants further investigation in future studies.

Conclusions

Our study, conducted on two orthotopic colon cancer models of different genetic backgrounds, reveals that the development of colon cancer in mice leads to significant peripheral neuronal dysfunction, without prominent behavioral alterations. The observed neuronal changes are presumably induced by the prominent and complex inflammatory processes induced by tumor growth. The chemokines CCL2, CXCL1, CXCL2, and particularly CXCL10 might be key factors at play.

List Of Abbreviations

ATF-3 Activating transcription factor 3

BAFF B-cell activating factor/TNFSF13B

BCA Bicinchoninic acid

BSA Bovine serum albumin

CD14/68 Cluster of differentiation 14/68

CIPN Chemotherapy-induced peripheral neuropathy

CXCL1/2/5/9/10/16 C-X-C chemokine ligand 1/2/5/9/10/16

CCL2/3/4/5/6/11/12/17/19/20/22 C-C chemokine ligand 2/3/4/5/6/11/12/17/19/20/22

CMV Cytomegalovirus

CX3CL1 C-X3-C chemokine ligand 1/Fractalkine

DAPI 4',6-diamidino-2-phenylindole

DKK-1 Dickkopf WNT signaling pathway inhibitor 1

DRG Dorsal root ganglion

ECAR Extracellular acidification rate

EDTA Ethylenediaminetetraacetic acid

EGF Epidermal growth factor

FBS Fetal bovine serum

FCCP Carbonyl cyanide-p-trifluoromethoxyphenylhydrazone

FGF/-21 Fibroblast growth factor/-21

Flt-3 fms-like tyrosine kinase 3/CD135

Gas6 Growth arrest specific 6

G-CSF Granulocyte colony-stimulating factor

GDF-15 Growth/differentiation factor-15

GM-CSF Granulocyte-macrophage colony-stimulating factor

HEPES 4-(2-hydroxyethyl)-1-piperazineethanesulfonic acid

HGF Hepatocyte growth factor

HH HEPES-buffered Hanks' balanced salt solution

HRP Horseradish peroxidase

IENF Intra-epidermal nerve fiber

IFN- γ Interferon-gamma

IGFBP-1/3/6 Insulin-like growth factor-binding protein-1/3/6

IL-1 α /1 β /2/3/5/6/10/11/12p40 Interleukin-1 α /1 β /2/3/5/6/10/11/12p40
/13/17A/22/23/27p28/28A /13/17A/22/23/27p28/28A

IPA Ingenuity pathway analysis

LDL-R Low density lipoprotein receptor

LIF Leukemia inhibitory factor

M-CSF Macrophage colony-stimulating factor

MMP-3/9 Matrix metalloproteinase-3/9

NF200 Neurofilament 200

OCR Oxygen consumption rate

PB Phosphate buffer

PBS Phosphate-buffered saline

PCSK9 Proprotein convertase subtilisin/kexin type 9

PD-ECGF Platelet-derived endothelial cell growth factor

PDGF-BB Platelet-derived growth factor-BB

PFA Paraformaldehyde

PGP9.5 Protein gene product 9.5

Pref-1 Preadipocyte factor-1

RAGE Receptor for advanced glycation endproducts

RBP4 Retinol binding protein-4

Reg3G Regenerating islet-derived protein III-gamma

SEM Standard error of the mean

SERCA Sarco/endoplasmic reticulum Ca²⁺ ATPase

TIM-1 T cell immunoglobulin and mucin domain-1

TNF-α Tumor necrosis factor-alpha

VCAM-1/CD106 Vascular cell adhesion protein-1

VEGF Vascular endothelial growth factor

Declarations

Ethics approval and consent to participate: Not applicable

Consent for publication: Not applicable

Availability of data and material: The datasets used and analyzed during the current study are available from the corresponding author on reasonable request.

Competing interests: The authors declare that they have no competing interests.

Funding: This work was funded by the Rita Allen Foundation, an MD Anderson Cyrus Scholar award and Institutional Research Grant funding (to AJS).

Authors' contributions: MB performed mouse injections, imaging, IHC and microscopy and wrote the first draft of the manuscript. JZ performed Seahorse analysis. CMG, NK and NTN performed behavioral and *in vitro* experiments. CA generated and validated MC38 cells stably expressing luciferase. HVP, BM and JMN provided technical assistance. RTT prepared samples for RNAseq. RM analyzed and interpreted RNAseq data. AJS conceptualized the study and edited the manuscript. All authors read and approved the final manuscript.

Acknowledgements: We wish to thank Dr. Annemieke Kavelaars for her constructive criticism of this project throughout its development.

References

1. Kuipers EJ, Grady WM, Lieberman D, Seufferlein T, Sung JJ, Boelens PG, et al. Colorectal cancer. *Nat Rev Dis Prim* [Internet]. Nature Publishing Group; 2015 [cited 2021 Jul 23];1:15065. Available from: [/pmc/articles/PMC4874655/](https://pubmed.ncbi.nlm.nih.gov/25530442/)
2. Naghavi M, Wang H, Lozano R, Davis A, Liang X, Zhou M, et al. Global, regional, and national age-sex specific all-cause and cause-specific mortality for 240 causes of death, 1990–2013: A systematic analysis for the Global Burden of Disease Study 2013. *Lancet* [Internet]. 2015;385:117–71. Available from: <http://www.ncbi.nlm.nih.gov/pubmed/25530442><http://www.pubmedcentral.nih.gov/articlerender.fcgi?artid=PMC4340604>
3. Siegel RL, Miller KD, Fuchs HE, Jemal A. Cancer Statistics, 2021. *CA Cancer J Clin* [Internet]. Wiley; 2021 [cited 2021 Jul 23];71:7–33. Available from: <https://pubmed.ncbi.nlm.nih.gov/33433946/>
4. Bouchenaki H, Danigo A, Sturtz F, Hajj R, Magy L, Demiot C. An overview of ongoing clinical trials assessing pharmacological therapeutic strategies to manage chemotherapy-induced peripheral neuropathy, based on preclinical studies in rodent models [Internet]. *Fundam. Clin. Pharmacol.* Blackwell Publishing Ltd; 2021 [cited 2021 Jul 23]. p. 506–23. Available from: <https://pubmed.ncbi.nlm.nih.gov/33107619/>
5. Chung JW, Cho YH, Ahn MJ, Lee MJ, Kim GM, Chung CS, et al. Association of cancer cell type and extracellular vesicles with coagulopathy in patients with lung cancer and stroke. *Stroke* [Internet]. Lippincott Williams and Wilkins; 2018 [cited 2022 Apr 28];49:1282–5. Available from: <https://www.ahajournals.org/doi/abs/10.1161/STROKEAHA.118.020995>
6. Munn LL. Cancer and inflammation. *Wiley Interdiscip Rev Syst Biol Med* [Internet]. Wiley-Blackwell; 2017 [cited 2021 Jan 11];9:e1370. Available from: <http://doi.wiley.com/10.1002/wsbm.1370>
7. Aloyouny AY, Bepari A, Rahman I. Evaluating the role of CXCR3 in pain modulation: A literature review [Internet]. *J. Pain Res.* Dove Medical Press Ltd.; 2020 [cited 2021 Jul 23]. p. 1987–2001. Available from: <https://pubmed.ncbi.nlm.nih.gov/32821152/>

8. Giorgio C, Zippoli M, Cocchiaro P, Castelli V, Varrassi G, Aramini A, et al. Emerging role of C5 complement pathway in peripheral neuropathies: Current treatments and future perspectives [Internet]. *Biomedicines*. MDPI AG; 2021 [cited 2021 Jul 23]. Available from: <https://pubmed.ncbi.nlm.nih.gov/33917266/>
9. Allen F, Bobanga ID, Rauhe P, Barkauskas D, Teich N, Tong C, et al. CCL3 augments tumor rejection and enhances CD8 + T cell infiltration through NK and CD103 + dendritic cell recruitment via IFN γ . *Oncoimmunology* [Internet]. Taylor and Francis Inc.; 2018 [cited 2021 Jul 23];7. Available from: <https://pubmed.ncbi.nlm.nih.gov/29399390/>
10. Piao C, Cai L, Qiu S, Jia L, Song W, Du J. Complement 5a enhances hepatic metastases of colon cancer via monocyte chemoattractant protein-1-mediated inflammatory cell infiltration. *J Biol Chem* [Internet]. American Society for Biochemistry and Molecular Biology Inc.; 2015 [cited 2021 Jul 23];290:10667–76. Available from: </pmc/articles/PMC4409234/>
11. Deng S, Deng Q, Zhang Y, Ye H, Yu X, Zhang Y, et al. Non-platelet-derived CXCL4 differentially regulates cytotoxic and regulatory T cells through CXCR3 to suppress the immune response to colon cancer. *Cancer Lett* [Internet]. Elsevier Ireland Ltd; 2019 [cited 2021 Jul 23];443:1–12. Available from: <https://pubmed.ncbi.nlm.nih.gov/30481563/>
12. Lepsenyi M, Algethami N, Al-Haidari AA, Algaber A, Syk I, Rahman M, et al. CXCL2-CXCR2 axis mediates α V integrin-dependent peritoneal metastasis of colon cancer cells. *Clin Exp Metastasis* [Internet]. Springer Science and Business Media B.V.; 2021 [cited 2021 Jul 23]; Available from: <https://pubmed.ncbi.nlm.nih.gov/34115261/>
13. Piao C, Zhang WM, Li TT, Zhang C cong, Qiu S, Liu Y, et al. Complement 5a stimulates macrophage polarization and contributes to tumor metastases of colon cancer. *Exp Cell Res* [Internet]. Elsevier Inc.; 2018 [cited 2021 Jul 23];366:127–38. Available from: <https://pubmed.ncbi.nlm.nih.gov/29551360/>
14. Monje M, Borniger JC, D’Silva NJ, Deneen B, Dirks PB, Fattahi F, et al. Roadmap for the Emerging Field of Cancer Neuroscience. *Cell*. Cell Press; 2020;181:219–22.
15. Hean V, Camdessanché JP, Cathébras P, Killian M. Paraneoplastic subacute sensory neuropathy with triple positive antineuronal antibodies associated with small-cell lung cancer. *BMJ Case Rep* [Internet]. BMJ Specialist Journals; 2020 [cited 2022 Apr 28];13:e235668. Available from: <https://casereports.bmj.com/content/13/8/e235668>
16. Koike H, Tanaka F, Sobue G. Paraneoplastic neuropathy: Wide-ranging clinicopathological manifestations. *Curr Opin Neurol* [Internet]. 2011 [cited 2022 Apr 28];24:504–10. Available from: https://journals.lww.com/co-neurology/Fulltext/2011/10000/Paraneoplastic_neuropathy__wide_ranging.15.aspx
17. Colvin LA. Chemotherapy-induced peripheral neuropathy: Where are we now? [Internet]. *Pain*. Lippincott Williams and Wilkins; 2019 [cited 2021 Jan 11]. p. S1–10. Available from: </pmc/articles/PMC6499732/?report=abstract>
18. EGFP (CAG) Lentivirus - Kerfast [Internet]. [cited 2021 May 26]. Available from: <https://www.kerfast.com/productgroup/475/egfp-cag-lentivirus>
19. Protocol QR. G418 Sulfate Solution [Internet]. Available from: <https://www.mirusbio.com/products/accessories/selection-antibiotics>
20. Donigan M, Loh BD, Norcross LS, Li S, Williamson PR, DeJesus S, et al. A metastatic colon cancer model using nonoperative transanal rectal injection. *Surg Endosc* [Internet]. Springer New York; 2010 [cited 2021

- Jul 26];24:642–7. Available from: <https://link.springer.com/article/10.1007/s00464-009-0650-9>
21. Shepherd AJ, Copits BA, Mickle AD, Karlsson P, Kadunganattil S, Haroutounian S, et al. Angiotensin II triggers peripheral macrophage-to-sensory neuron redox crosstalk to elicit pain. *J Neurosci. Society for Neuroscience*; 2018;38:7032–57.
 22. Dorninger F, Zeitler G, Berger J. Nestlet Shredding and Nest Building Tests to Assess Features of Psychiatric Disorders in Mice. *BIO-PROTOCOL* [Internet]. Bio-Protocol, LLC; 2020 [cited 2021 May 10];10. Available from: <https://pubmed.ncbi.nlm.nih.gov/33473360/>
 23. Angoa-Pérez M, Kane MJ, Briggs DI, Francescutti DM, Kuhn DM. Marble burying and nestlet shredding as tests of repetitive, compulsive-like behaviors in mice. *J Vis Exp* [Internet]. MyJoVE Corporation; 2013 [cited 2021 Jul 21];82:50978. Available from: </pmc/articles/PMC4108161/>
 24. Murphy M, Mills S, Winstone J, Leishman E, Wager-Miller J, Bradshaw H, et al. Chronic Adolescent Δ^9 -Tetrahydrocannabinol Treatment of Male Mice Leads to Long-Term Cognitive and Behavioral Dysfunction, Which Are Prevented by Concurrent Cannabidiol Treatment. *Cannabis Cannabinoid Res* [Internet]. Mary Ann Liebert Inc; 2017 [cited 2021 Jul 21];2:235–46. Available from: </pmc/articles/PMC5655843/>
 25. Suzuki M, Narita M, Hasegawa M, Furuta S, Kawamata T, Ashikawa M, et al. Sensation of abdominal pain induced by peritoneal carcinomatosis is accompanied by changes in the expression of substance p and μ -opioid receptors in the spinal cord of mice. *Anesthesiology. The American Society of Anesthesiologists*; 2012;117:847–56.
 26. Bouet V, Boulouard M, Toutain J, Divoux D, Bernaudin M, Schumann-Bard P, et al. The adhesive removal test: A sensitive method to assess sensorimotor deficits in mice. *Nat Protoc* [Internet]. Nature Publishing Group; 2009 [cited 2022 Apr 28];4:1560–4. Available from: <https://www.nature.com/articles/nprot.2009.125>
 27. Chaplan SR, Bach FW, Pogrel JW, Chung JM, Yaksh TL. Quantitative assessment of tactile allodynia in the rat paw. *J Neurosci Methods* [Internet]. *J Neurosci Methods*; 1994 [cited 2021 Feb 4];53:55–63. Available from: <https://pubmed.ncbi.nlm.nih.gov/7990513/>
 28. Krukowski K, Ma J, Golonzhka O, Laumet GO, Gutti T, Van Duzer JH, et al. HDAC6 inhibition effectively reverses chemotherapy-induced peripheral neuropathy. *Pain* [Internet]. NIH Public Access; 2017 [cited 2021 May 27];158:1126–37. Available from: </pmc/articles/PMC5435512/>
 29. Garriga J, Laumet G, Chen SR, Zhang Y, Madzo J, Issa JPJ, et al. Nerve injury-induced chronic pain is associated with persistent DNA methylation reprogramming in dorsal root ganglion. *J Neurosci* [Internet]. Society for Neuroscience; 2018 [cited 2021 May 27];38:6090–101. Available from: </pmc/articles/PMC6031579/>
 30. Brenner DS, Golden JP, Gereau IV RW. A novel behavioral assay for measuring cold sensation in mice. Sakakibara M, editor. *PLoS One* [Internet]. Public Library of Science; 2012 [cited 2021 Feb 4];7:e39765. Available from: <https://dx.plos.org/10.1371/journal.pone.0039765>
 31. Shepherd AJ, Loo L, Mohapatra DP. Chemokine Co-Receptor CCR5/CXCR4-Dependent Modulation of Kv2.1 Channel Confers Acute Neuroprotection to HIV-1 Glycoprotein gp120 Exposure. *PLoS One* [Internet]. Public Library of Science; 2013 [cited 2021 Jul 21];8. Available from: </pmc/articles/PMC3782454/>
 32. Shepherd AJ, Loo L, Gupte RP, Mickle AD, Mohapatra DP. Distinct modifications in Kv2.1 channel via chemokine receptor CXCR4 regulate neuronal survival-death dynamics. *J Neurosci* [Internet]. Society for Neuroscience; 2012 [cited 2021 Jul 21];32:17725–39. Available from: </pmc/articles/PMC3544972/>

33. Shepherd AJ, Mohapatra DP. Tissue preparation and immunostaining of mouse sensory nerve fibers innervating skin and limb bones. *J Vis Exp* [Internet]. Journal of Visualized Experiments; 2012 [cited 2021 Jul 26];1–6. Available from: <https://www.jove.com/v/3485/tissue-preparation-immunostaining-mouse-sensory-nerve-fibers>
34. Nichols JM, Crelli C V., Liu L, Pham HV, Janjic JM, Shepherd AJ. Tracking macrophages in diabetic neuropathy with two-color nanoemulsions for near-infrared fluorescent imaging and microscopy. *J Neuroinflammation* [Internet]. BioMed Central Ltd; 2021 [cited 2022 Apr 28];18:1–22. Available from: <https://link.springer.com/articles/10.1186/s12974-021-02365-y>
35. Maj MA, Ma J, Krukowski KN, Kavelaars A, Heijnen CJ. Inhibition of mitochondrial p53 accumulation by PFT- μ prevents cisplatin-induced peripheral neuropathy. *Front Mol Neurosci* [Internet]. Frontiers Research Foundation; 2017 [cited 2021 Jul 21];10:108. Available from: <http://journal.frontiersin.org/article/10.3389/fnmol.2017.00108/full>
36. Krukowski K, Nijboer CH, Huo X, Kavelaars A, Heijnen CJ. Prevention of chemotherapy-induced peripheral neuropathy by the small-molecule inhibitor pifithrin- μ . *Pain* [Internet]. Lippincott Williams and Wilkins; 2015 [cited 2021 Jul 21];156:2184–92. Available from: </pmc/articles/PMC4900465/>
37. McArthur JC, Stocks EA, Hauer P, Cornblath DR, Griffin JW. Epidermal nerve fiber density: Normative reference range and diagnostic efficiency. *Arch Neurol* [Internet]. American Medical Association; 1998 [cited 2021 Jul 27];55:1513–20. Available from: <https://pubmed.ncbi.nlm.nih.gov/9865794/>
38. Ma J, Farmer KL, Pan P, Urban MJ, Zhao H, Blagg BSJ, et al. Heat shock protein 70 is necessary to improve mitochondrial bioenergetics and reverse diabetic sensory neuropathy following KU-32 therapy. *J Pharmacol Exp Ther* [Internet]. American Society for Pharmacology and Experimental Therapeutics; 2014 [cited 2021 Jul 21];348:281–92. Available from: <http://dx.doi.org/10.1124/jpet.113.210435>
39. Ma J, Trinh RT, Mahant ID, Peng B, Matthias P, Heijnen CJ, et al. Cell-specific role of histone deacetylase 6 in chemotherapy-induced mechanical allodynia and loss of intraepidermal nerve fibers. *Pain* [Internet]. Lippincott Williams and Wilkins; 2019 [cited 2021 Jul 21];160:2877–90. Available from: </pmc/articles/PMC6856416/>
40. Loo L, Shepherd AJ, Mickle AD, Lorca RA, Shutov LP, Usachev YM, et al. The C-type natriuretic peptide induces thermal hyperalgesia through a noncanonical G $\beta\gamma$ -dependent modulation of TRPV1 channel. *J Neurosci* [Internet]. Society for Neuroscience; 2012 [cited 2021 Oct 6];32:11942–55. Available from: <https://www.jneurosci.org/content/32/35/11942>
41. Davidson S, Golden JP, Copits BA, Ray PR, Vogt SK, Valtcheva M V., et al. Group II mGluRs suppress hyperexcitability in mouse and human nociceptors. *Pain* [Internet]. Lippincott Williams and Wilkins; 2016 [cited 2021 Oct 6];157:2081–8. Available from: </pmc/articles/PMC4988887/>
42. Malin SA, Davis BM, Molliver DC. Production of dissociated sensory neuron cultures and considerations for their use in studying neuronal function and plasticity. *Nat Protoc* [Internet]. Nature Publishing Group; 2007 [cited 2022 Apr 28];2:152–60. Available from: <https://www.nature.com/articles/nprot.2006.461>
43. English K, Shepherd A, Uzor NE, Trinh R, Kavelaars A, Heijnen CJ. Astrocytes rescue neuronal health after cisplatin treatment through mitochondrial transfer. *Acta Neuropathol Commun* [Internet]. BioMed Central Ltd.; 2020 [cited 2021 Sep 2];8:1–14. Available from: <https://link.springer.com/articles/10.1186/s40478-020-00897-7>

44. Singhmar P, Trinh RTP, Ma J, Huo XJ, Peng B, Heijnen CJ, et al. The fibroblast-derived protein PI16 controls neuropathic pain. *Proc Natl Acad Sci U S A* [Internet]. National Academy of Sciences; 2020 [cited 2022 Feb 1];117:5463–71. Available from: [/pmc/articles/PMC7071920/](https://pubmed.ncbi.nlm.nih.gov/26334920/)
45. Simon Andrews. Babraham Bioinformatics - FastQC A Quality Control tool for High Throughput Sequence Data [Internet]. *Soil*. 2020 [cited 2022 Feb 1]. p. 47–81. Available from: <https://www.bioinformatics.babraham.ac.uk/projects/fastqc/>
46. Dobin A, Gingeras TR. Mapping RNA-seq Reads with STAR. *Curr Protoc Bioinforma* [Internet]. John Wiley and Sons Inc.; 2015 [cited 2022 Feb 1];51:11.14.1-11.14.19. Available from: <https://pubmed.ncbi.nlm.nih.gov/26334920/>
47. Liao Y, Smyth GK, Shi W. The Subread aligner: Fast, accurate and scalable read mapping by seed-and-vote. *Nucleic Acids Res* [Internet]. *Nucleic Acids Res*; 2013 [cited 2022 Feb 1];41. Available from: <https://pubmed.ncbi.nlm.nih.gov/23558742/>
48. Love MI, Huber W, Anders S. Moderated estimation of fold change and dispersion for RNA-seq data with DESeq2. *Genome Biol* [Internet]. BioMed Central Ltd.; 2014 [cited 2022 Feb 1];15. Available from: <https://pubmed.ncbi.nlm.nih.gov/25516281/>
49. Proteome Profiler Mouse Cytokine Array Kit, Panel A (ARY006): R&D Systems [Internet]. [cited 2021 Jul 21]. Available from: https://www.rndsystems.com/products/proteome-profiler-mouse-xl-cytokine-array_ary028
50. Brierley SM, Hibberd TJ, Spencer NJ. Spinal afferent innervation of the colon and rectum. *Front. Cell. Neurosci. Frontiers Media S.A.*; 2018. p. 467.
51. Xian H, Xie R, Luo C, Cong R. Comparison of Different in Vivo Animal Models of Brachial Plexus Avulsion and Its Application in Pain Study. *Neural Plast. Hindawi Limited*; 2020.
52. Zhang H, Li Y, De Carvalho-Barbosa M, Kavelaars A, Heijnen CJ, Albrecht PJ, et al. Dorsal Root Ganglion Infiltration by Macrophages Contributes to Paclitaxel Chemotherapy-Induced Peripheral Neuropathy. *J Pain. Churchill Livingstone*; 2016;17:775–86.
53. Branca JJV, Carrino D, Gulisano M, Ghelardini C, Di Cesare Mannelli L, Pacini A. Oxaliplatin-Induced Neuropathy: Genetic and Epigenetic Profile to Better Understand How to Ameliorate This Side Effect [Internet]. *Front. Mol. Biosci. Frontiers Media S.A.*; 2021 [cited 2021 Jul 23]. Available from: [/pmc/articles/PMC8138476/](https://pubmed.ncbi.nlm.nih.gov/34138476/)
54. Di Cesare Mannelli L, Pacini A, Bonaccini L, Zanardelli M, Mello T, Ghelardini C. Morphologic features and glial activation in rat oxaliplatin-dependent neuropathic pain. *J Pain* [Internet]. *J Pain*; 2013 [cited 2021 Jul 27];14:1585–600. Available from: <https://pubmed.ncbi.nlm.nih.gov/24135431/>
55. Starobova H, Vetter I. Pathophysiology of chemotherapy-induced peripheral neuropathy. *Front. Mol. Neurosci. Frontiers Media S.A.*; 2017.
56. Hamilton J, Brustovetsky T, Rysted JE, Lin Z, Usachev YM, Brustovetsky N. Deletion of mitochondrial calcium uniporter incompletely inhibits calcium uptake and induction of the permeability transition pore in brain mitochondria. *J Biol Chem* [Internet]. Elsevier; 2018 [cited 2022 Apr 28];293:15652–63. Available from: <http://www.jbc.org/article/S0021925820352662/fulltext>
57. Zhou L, Ao L, Yan Y, Li W, Ye A, Hu Y, et al. The Therapeutic Potential of Chemokines in the Treatment of Chemotherapy- Induced Peripheral Neuropathy. *Curr Drug Targets* [Internet]. Bentham Science Publishers Ltd.; 2019 [cited 2021 Aug 16];21:288–301. Available from: <https://pubmed.ncbi.nlm.nih.gov/31490748/>

58. Kawai K, Watanabe T. Colorectal cancer and hypercoagulability. *Surg Today* [Internet]. Springer-Verlag Tokyo; 2014 [cited 2022 May 12];44:797–803. Available from: <https://link.springer.com/article/10.1007/s00595-013-0606-5>
59. Denlinger CS, Barsevick AM. The challenges of colorectal cancer survivorship. *JNCCN J Natl Compr Cancer Netw* [Internet]. Harborside Press, LLC; 2009 [cited 2022 May 12];7:883–94. Available from: <https://jnccn.org/view/journals/jnccn/7/8/article-p883.xml>
60. Boyette-Davis JA, Eng C, Wang XS, Cleeland CS, Wendelschafer-Crabb G, Kennedy WR, et al. Subclinical peripheral neuropathy is a common finding in colorectal cancer patients prior to chemotherapy. *Clin Cancer Res* [Internet]. *Clin Cancer Res*; 2012 [cited 2021 Jul 23];18:3180–7. Available from: <https://pubmed.ncbi.nlm.nih.gov/22496202/>
61. Gregory NS, Harris AL, Robinson CR, Dougherty PM, Fuchs PN, Sluka KA. An overview of animal models of pain: Disease models and outcome measures [Internet]. *J. Pain*. 2013 [cited 2018 Feb 9]. p. 1255–69. Available from: <https://www.ncbi.nlm.nih.gov/pmc/articles/PMC3818391/pdf/nihms504077.pdf>
62. Flatters SJL, Dougherty PM, Colvin LA. Clinical and preclinical perspectives on Chemotherapy-Induced Peripheral Neuropathy (CIPN): A narrative review [Internet]. *Br. J. Anaesth.* Oxford University Press; 2017 [cited 2021 Jul 23]. p. 737–49. Available from: <https://pubmed.ncbi.nlm.nih.gov/29121279/>
63. Koskinen MJ, Kautio AL, Haanpää ML, Haapasalo HK, Kellokumpu-Lehtinen PL, Saarto T, et al. Intraepidermal nerve fibre density in cancer patients receiving adjuvant chemotherapy. *Anticancer Res* [Internet]. 2011 [cited 2021 Jul 23];31:4413–6. Available from: <https://pubmed.ncbi.nlm.nih.gov/22199308/>
64. Sorensen L, Molyneaux L, Yue DK. The relationship among pain, sensory loss, and small nerve fibers in diabetes. *Diabetes Care* [Internet]. American Diabetes Association Inc.; 2006 [cited 2022 Jan 19];29:883–7. Available from: <http://diabetesjournals.org/care/article-pdf/29/4/883/561551/zdc00406000883.pdf>
65. Szabo-Pardi TA, Barron LR, Lenert ME, Burton MD. Sensory Neuron TLR4 mediates the development of nerve-injury induced mechanical hypersensitivity in female mice. *Brain Behav Immun.* Academic Press; 2021;97:42–60.
66. Lim TKY, Rone MB, Lee S, Antel JP, Zhang J. Mitochondrial and bioenergetic dysfunction in trauma-induced painful peripheral neuropathy. *Mol Pain* [Internet]. BioMed Central Ltd.; 2015 [cited 2022 May 12];11:58. Available from: <https://journals.sagepub.com/doi/full/10.1186/s12990-015-0057-7>
67. Collins P, Bing C, McCulloch P, Williams G. Muscle UCP-3 mRNA levels are elevated in weight loss associated with gastrointestinal adenocarcinoma in humans. *Br J Cancer* [Internet]. Nature Publishing Group; 2002 [cited 2022 May 12];86:372–5. Available from: <https://www.nature.com/articles/6600074>
68. Isaksson B, Rippe C, Simonoska R, Holm JE, Glaumann H, Segersvärd R, et al. Obstructive jaundice results in increased liver expression of uncoupling protein 2 and intact skeletal muscle glucose metabolism in the rat. *Scand J Gastroenterol* [Internet]. Taylor & Francis; 2002 [cited 2022 May 12];37:104–11. Available from: <https://www.tandfonline.com/doi/abs/10.1080/003655202753387446>
69. Kann O, Kovács R. Mitochondria and neuronal activity [Internet]. *Am. J. Physiol. - Cell Physiol.* American Physiological Society; 2007 [cited 2022 May 12]. p. 641–57. Available from: <https://journals.physiology.org/doi/full/10.1152/ajpcell.00222.2006>
70. Norat P, Soldozy S, Sokolowski JD, Gorick CM, Kumar JS, Chae Y, et al. Mitochondrial dysfunction in neurological disorders: Exploring mitochondrial transplantation [Internet]. *npj Regen. Med.* Nature Publishing

- Group; 2020 [cited 2022 May 12]. p. 1–9. Available from: <https://www.nature.com/articles/s41536-020-00107-x>
71. Roxburgh CSD, McMillan DC. Cancer and systemic inflammation: Treat the tumour and treat the host [Internet]. *Br. J. Cancer*. Nature Publishing Group; 2014 [cited 2022 May 12]. p. 1409–12. Available from: <https://www.nature.com/articles/bjc201490>
 72. Vichaya EG, Vermeer DW, Christian DL, Molkentine JM, Mason KA, Lee JH, et al. Neuroimmune mechanisms of behavioral alterations in a syngeneic murine model of human papilloma virus-related head and neck cancer. *Psychoneuroendocrinology*. Pergamon; 2017;79:59–66.
 73. Han CJ, Yang GS, Syrjala K. Symptom Experiences in Colorectal Cancer Survivors after Cancer Treatments: A Systematic Review and Meta-analysis [Internet]. *Cancer Nurs*. NIH Public Access; 2020 [cited 2022 May 12]. p. 132–58. Available from: </pmc/articles/PMC7182500/>
 74. Lopez ER, Carbajal AG, Tian J Bin, Bavencoffe A, Zhu MX, Dessauer CW, et al. Serotonin enhances depolarizing spontaneous fluctuations, excitability, and ongoing activity in isolated rat DRG neurons via 5-HT4 receptors and cAMP-dependent mechanisms. *Neuropharmacology*. Pergamon; 2021;184:108408.
 75. Rigaud M, Gemes G, Weyker PD, Cruikshank JM, Kawano T, Wu HE, et al. Axotomy depletes intracellular calcium stores in primary sensory neurons. *Anesthesiology* [Internet]. Lippincott Williams and Wilkins; 2009 [cited 2021 Dec 28];111:381–92. Available from: <http://pubs.asahq.org/anesthesiology/article-pdf/111/2/381/247013/0000542-200908000-00025.pdf>
 76. Hogan QH. Role of decreased sensory neuron membrane calcium currents in the genesis of neuropathic pain [Internet]. *Croat. Med. J.* 2007 [cited 2021 Dec 28]. p. 9–21. Available from: www.cmj.hr
 77. Fuchs A, Lirk P, Stucky C, Abram SE, Hogan QH. Painful nerve injury decreases resting cytosolic calcium concentrations in sensory neurons of rats. *Anesthesiology* [Internet]. American Society of Anesthesiologists; 2005 [cited 2021 Dec 28];102:1217–25. Available from: www.anesthesiology.org.
 78. Duncan C, Mueller S, Simon E, Renger JJ, Uebele VN, Hogan QH, et al. Painful nerve injury decreases sarcoplasmic reticulum Ca²⁺-ATPase activity in axotomized sensory neurons. *Neuroscience*. Pergamon; 2013;231:247–57.
 79. Gemes G, Rigaud M, Weyker PD, Abram SE, Weihrauch D, Poroli M, et al. Depletion of calcium stores in injured sensory neurons: Anatomic and functional correlates. *Anesthesiology* [Internet]. American Society of Anesthesiologists; 2009 [cited 2022 May 12];111:393–405. Available from: <https://pubs.asahq.org/anesthesiology/article/111/2/393/12229/Depletion-of-Calcium-Stores-in-Injured-Sensory>
 80. Hall BE, Macdonald E, Cassidy M, Yun S, Sapio MR, Ray P, et al. Transcriptomic Analysis of Human Sensory Neurons in Painful Diabetic Neuropathy Reveals Inflammation and Neuronal Loss. *bioRxiv* [Internet]. Cold Spring Harbor Laboratory; 2021 [cited 2022 Jan 20]; Available from: <https://doi.org/10.1101/2021.07.23.453576>
 81. Ferraz Gonçalves JA, Costa T, Rema J, Pinto C, Magalhães M, Esperança A, et al. Hypocalcemia in cancer patients: An exploratory study. *Porto Biomed J* [Internet]. Faculty of Medicine of the University of Porto; 2019 [cited 2022 May 12];4:e45. Available from: </pmc/articles/PMC6924975/>
 82. Duchon MR. Mitochondria and calcium: From cell signalling to cell death [Internet]. *J. Physiol*. Cambridge University Press; 2000 [cited 2022 Jan 20]. p. 57–68. Available from: </pmc/articles/PMC2270168/>

83. Yang Y, Luo L, Cai X, Fang Y, Wang J, Chen G, et al. Nrf2 inhibits oxaliplatin-induced peripheral neuropathy via protection of mitochondrial function. *Free Radic Biol Med*. Elsevier Inc.; 2018;120:13–24.
84. Fulkerson PC, Zimmermann N, Hassman LM, Finkelman FD, Rothenberg ME. Pulmonary Chemokine Expression Is Coordinately Regulated by STAT1, STAT6, and IFN- γ . *J Immunol* [Internet]. American Association of Immunologists; 2004 [cited 2022 May 12];173:7565–74. Available from: <https://www.jimmunol.org/content/173/12/7565>
85. Balkwill F. Cancer and the chemokine network [Internet]. *Nat. Rev. Cancer*. Nature Publishing Group; 2004 [cited 2022 Feb 1]. p. 540–50. Available from:
86. Yang X, Wei Y, Sheng F, Xu Y, Liu J, Gao L, et al. Comprehensive analysis of the prognosis and immune infiltration for CXC chemokines in colorectal cancer. *Aging (Albany NY)* [Internet]. Impact Journals LLC; 2021 [cited 2021 Aug 9];13:17548–67. Available from: </pmc/articles/PMC8312455/>
87. Iwasa T, Afroz S, Inoue M, Arakaki R, Oshima M, Raju R, et al. IL-10 and CXCL2 in trigeminal ganglia in neuropathic pain. *Neurosci Lett* [Internet]. Elsevier Ireland Ltd; 2019 [cited 2021 Aug 9];703:132–8. Available from: <https://pubmed.ncbi.nlm.nih.gov/30904573/>
88. Chen Y, Yin D, Fan B, Zhu X, Chen Q, Li Y, et al. Chemokine CXCL10/CXCR3 signaling contributes to neuropathic pain in spinal cord and dorsal root ganglia after chronic constriction injury in rats. *Neurosci Lett* [Internet]. Elsevier Ireland Ltd; 2019 [cited 2022 Feb 1];694:20–8. Available from: <https://pubmed.ncbi.nlm.nih.gov/30448292/>
89. Ju YY, Jiang M, Xu F, Wang D, Ding B, Ma LJ, et al. CXCL10 and CXCR3 in the trigeminal ganglion contribute to trigeminal neuropathic pain in mice. *J Pain Res* [Internet]. Dove Medical Press Ltd; 2021 [cited 2022 Feb 1];14:41–51. Available from: </pmc/articles/PMC7811485/>
90. Li HL, Huang Y, Zhou YL, Teng RH, Zhou SZ, Lin JP, et al. C-X-C Motif Chemokine 10 Contributes to the Development of Neuropathic Pain by Increasing the Permeability of the Blood–Spinal Cord Barrier. *Front Immunol* [Internet]. Frontiers Media S.A.; 2020 [cited 2022 Feb 1];11:477. Available from: </pmc/articles/PMC7098954/>
91. Missiroli S, Genovese I, Perrone M, Vezzani B, Vitto VAM, Giorgi C. The role of mitochondria in inflammation: From cancer to neurodegenerative disorders [Internet]. *J. Clin. Med*. Multidisciplinary Digital Publishing Institute; 2020 [cited 2022 May 12]. p. 740. Available from: <https://www.mdpi.com/2077-0383/9/3/740/htm>
92. Kosturakis AK, He Z, Li Y, Boyette-Davis JA, Shah N, Thomas SK, et al. Subclinical peripheral neuropathy in patients with multiple myeloma before chemotherapy is correlated with decreased fingertip innervation density. *J Clin Oncol* [Internet]. American Society of Clinical Oncology; 2014 [cited 2022 Apr 28];32:3156–62. Available from: </pmc/articles/PMC4171359/>

Figures

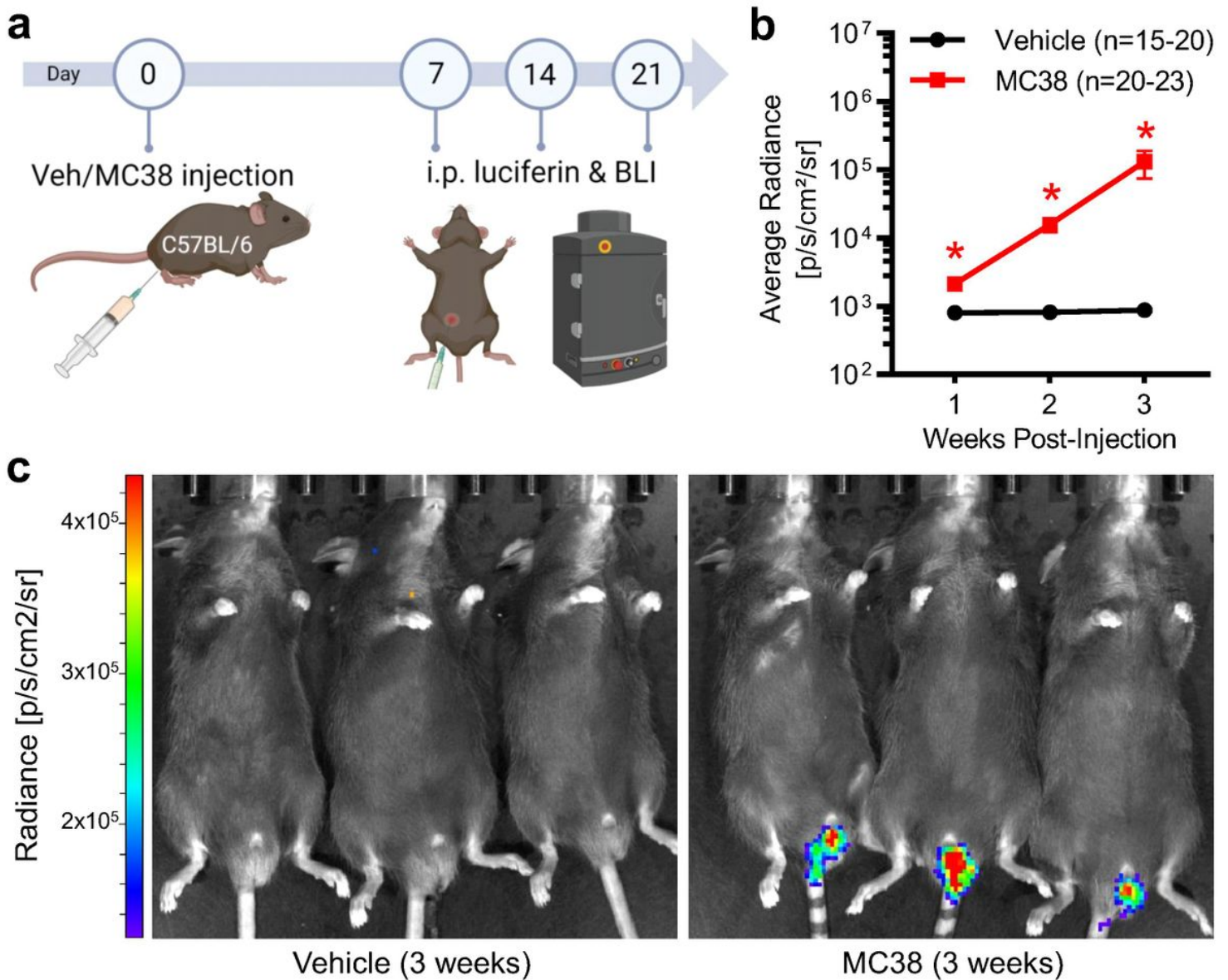


Figure 1

In vivo bioluminescence imaging of colon cancer development after local MC38 cell injection

Panel a: schematic depicting of experimental protocol for IVIS bioluminescence measurements (animals were measured 7, 14, and 21 days after vehicle/MC38 cell injection). **Panel b:** changes in average bioluminescence radiance values. The consistent localized increase in the measured bioluminescence signal relates to consistent tumor growth after the transanal MC38 cell injection. *: $p < 0.05$ vs control. **Panel c:** representative image of three control (vehicle injected) and colon cancer bearing (MC38 injected) mice, 3 weeks after inoculation.

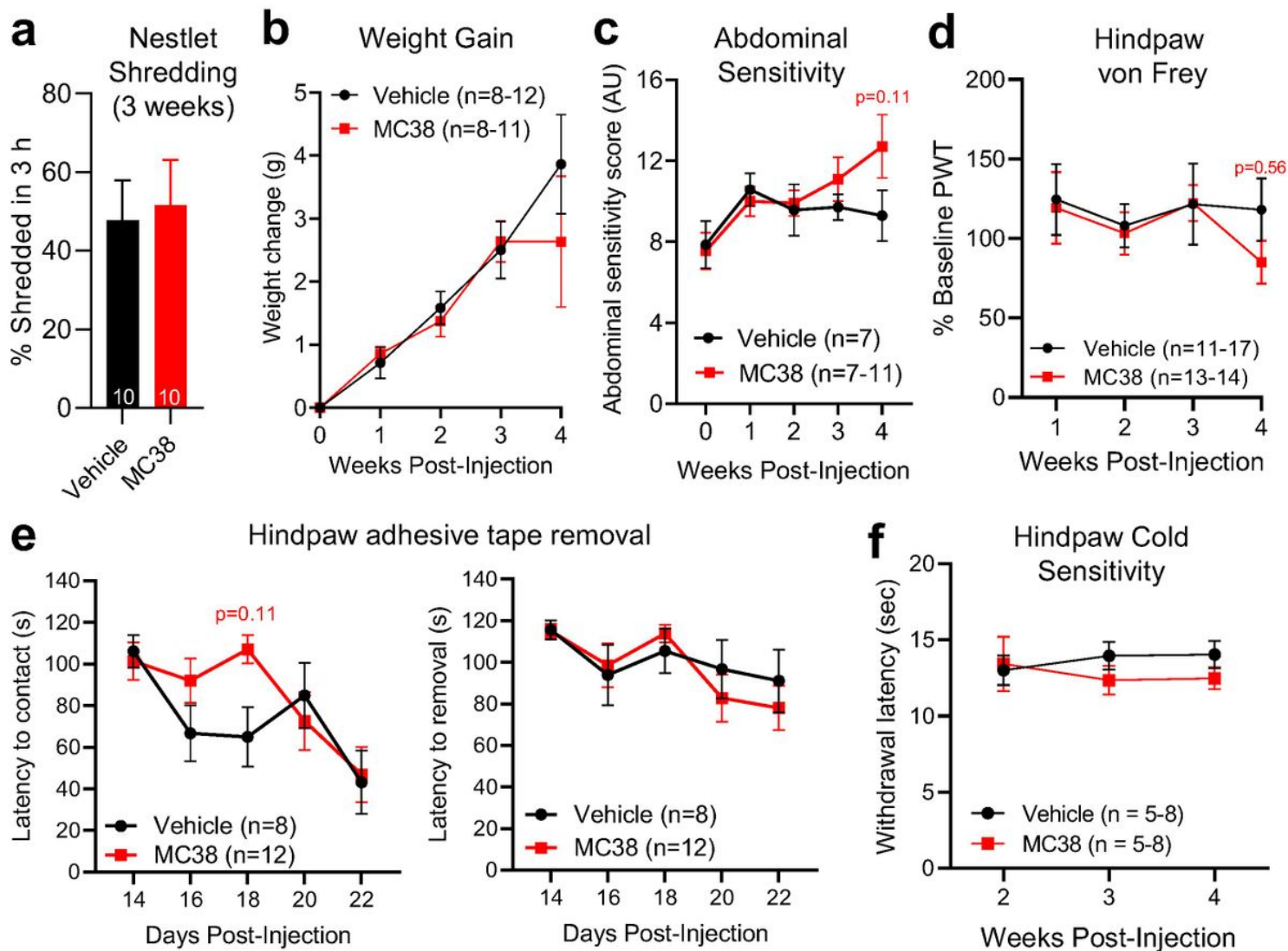


Figure 2

Animal well-being- and pain-related behavior tests in the MC38 colon cancer model

Panel a: Nestlet shredding assay. Columns depict percentage of shredded nestlet after the 3 h experimental time period. No change in the nestlet shredding indicates proper physiological behavior. **Panel b:** Weight gain (g) of vehicle vs MC38 injected mice after inoculation (compared to baseline at week 0, before injection). Data shows no significant difference in the growth of mice with or without colon cancer. **Panel c:** Changes in abdominal sensitivity of vehicle vs MC38 injected mice after inoculation. The graph shows the scored response provoked by the application of the 0.02 g Von Frey filament to the abdominal surface **Panel d:** Mechanical sensitivity of hind paws, as measured by the application of von Frey filaments, by the up-and-down method. Datapoints represent the average of percentage changes, as compared to the measured individual baseline values (measured at week 0, before inoculation). Animals did not develop significant mechanical allodynia. **Panel e:** Changes in the removal of adhesive tape, depicted as latency to contact (sec), and latency to removal (sec), respectively. Animals with colon cancer did not develop elevated tactile sensitivity. **Panel f:** Cold sensitivity of hind paws. Withdrawal threshold: time until sudden removal of the hind paw (sec). The induction of colon cancer did not result in elevated cold sensitivity in the experimental period.

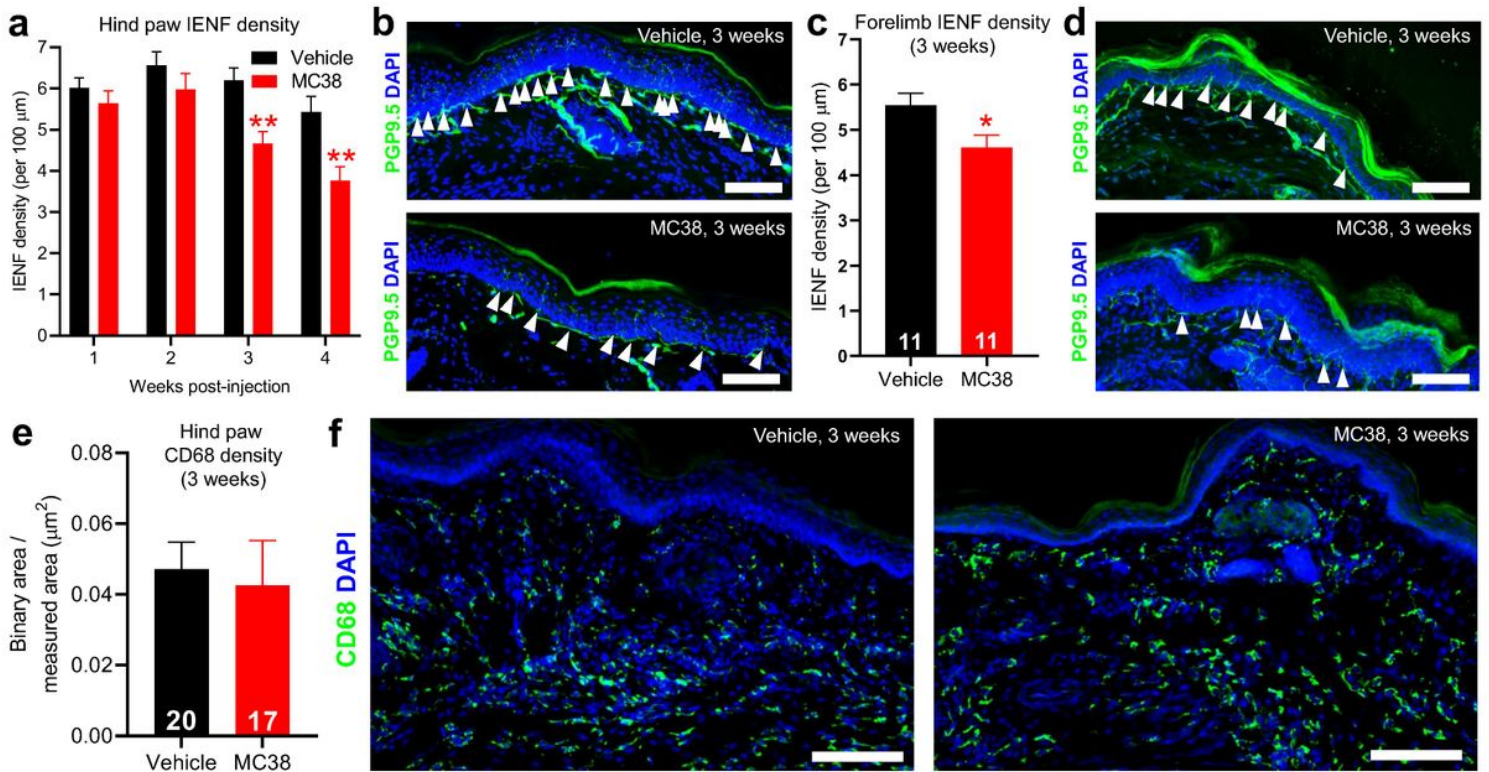


Figure 3

IHC assessment of hind paw and forelimb samples after MC38 injection

Panel a: Changes in IENF density with time in the hind paws of control vs MC38 injected mice. Colon cancer initiates a significant decrease in IENF density after the 3rd week, indicating significant neuronal damage. (**: $p < 0.01$; $n = 9-13$ /group) **Panel b:** Representative images of hind paw samples, collected 3 weeks after inoculation. White arrows mark the counted intraepidermal nerve fibers, stained with PGP9.5 antibody (green). Nuclei are stained with DAPI (blue). Scale bar: 100 μm **Panel c:** Changes in IENF density, 3 weeks after inoculation, in the forelimb samples of control vs MC38 injected mice. Similarly to the hind paw samples, our data reveals a significant decrease in IENF density, 3 weeks after local MC38 cell injection. **Panel d:** Representative images of forelimb samples, collected 3 weeks after tumor inoculation. White arrows mark the counted intraepidermal nerve fibers marked by PGP9.5 antibody. Nuclei are stained with DAPI. **Panel e:** Signal intensity of the CD68 macrophage marker in the skin of control vs MC38 injected mice, depicted as binary area/measured area. Based on the CD68 marker, there is no significant change in the number of macrophages in the epidermis, around the intraepidermal nerve fibers. **Panel f:** representative images of hind paw samples show no change in the CD68 signal intensity of the epidermis. Nuclei are stained with DAPI. Scale bar: 100 μm.

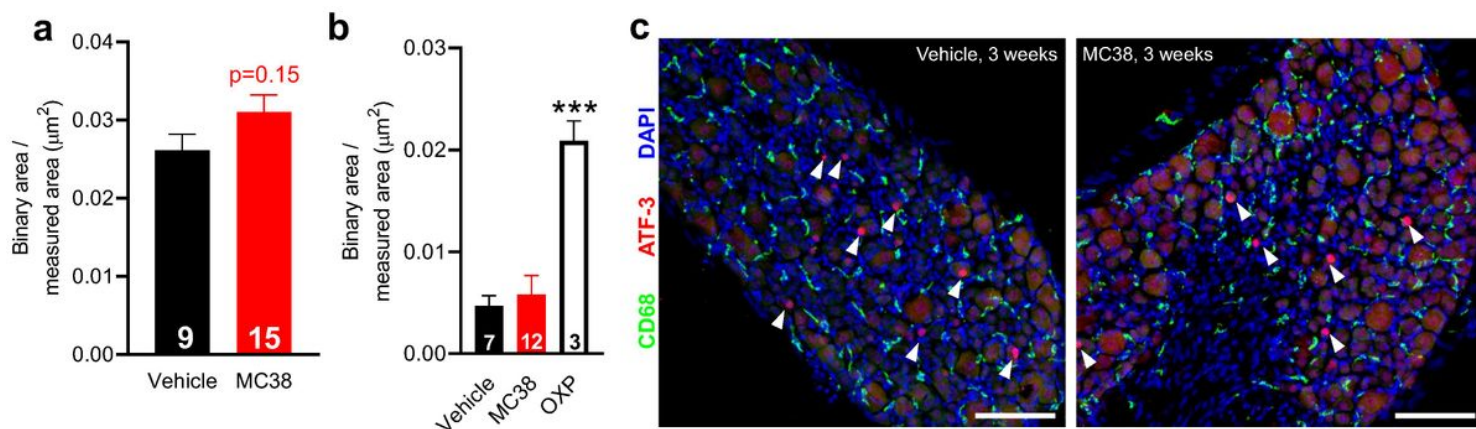


Figure 4

IHC assessment of the neuronal damage marker ATF-3 in DRGs

Lumbar DRG samples were collected 3 weeks after tumor inoculation. **Panel a:** No change in the signal intensity of the neuronal damage marker ATF-3 (vehicle vs MC38 injected mice). **Panel b:** same data set, with the addition of samples from oxaliplatin treated mice, as positive control (cumulative dose: 12 mg/kg i.p. in 3 days). Oxaliplatin treatment causes neuronal damage, hence significantly elevates the ATF-3 signal intensity, as expected. **Panel c:** representative images show no change in ATF-3 signal (samples from a vehicle vs an MC38 injected mouse, collected 3 weeks after injection). White arrows indicate cells positive for ATF-3. Scale bar: 100 µm. ***=p<.001, one-way ANOVA, Bonferroni.

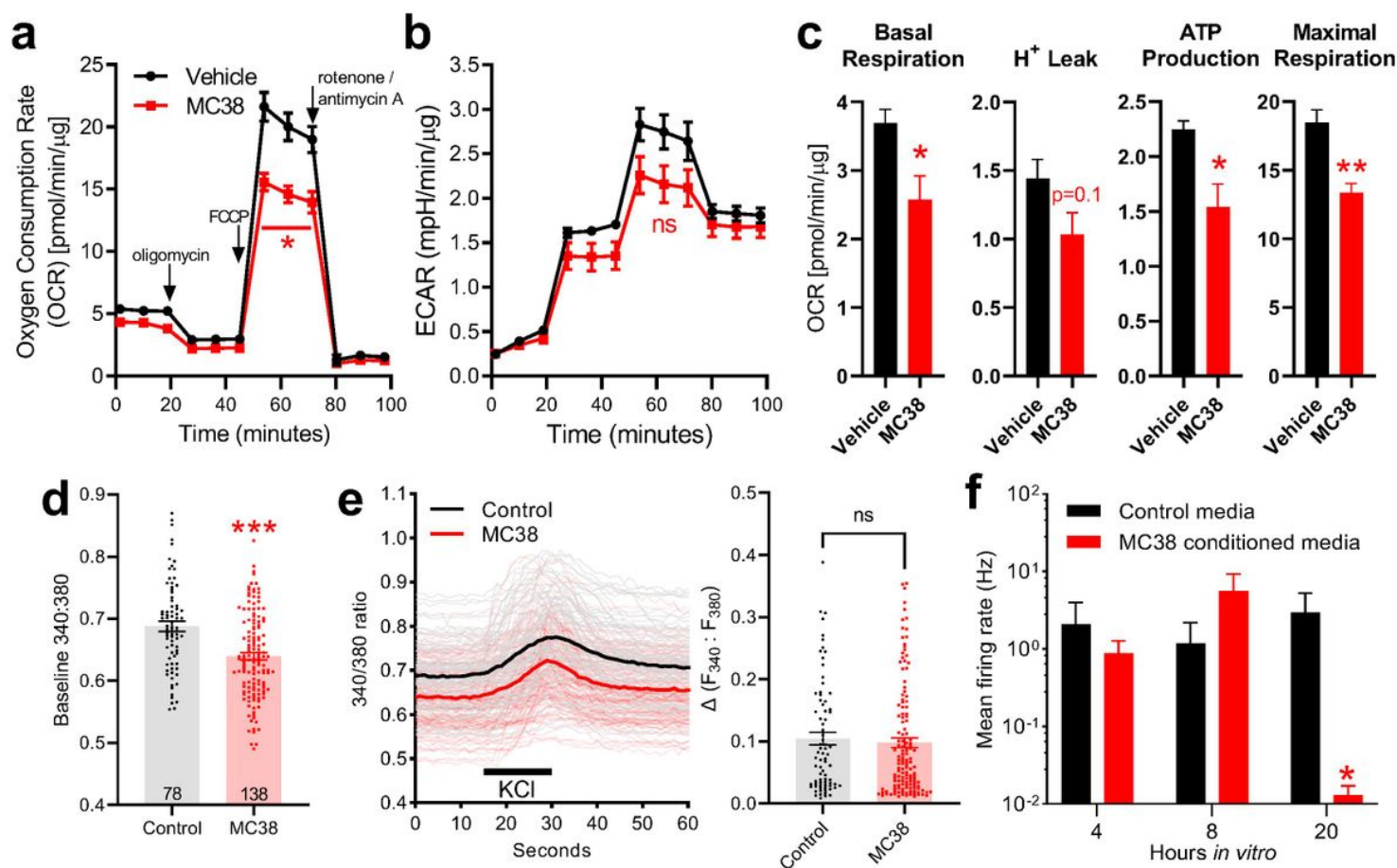


Figure 5

Mitochondrial function, Ca²⁺ homeostasis and spontaneous activity of lumbar DRG neurons

Panels a-c: Mitochondrial function assay (n= 3/group, in duplicates) on DRGs collected 3 weeks after inoculation. All values are normalized to mitochondrial-dependent respiration and the protein load. The assay revealed a significant dysfunction in animals with colon cancer. **Panel a:** Differences in oxygen consumption rate (OCR). **Panel b:** Differences in extracellular acidification rate (ECAR). **Panel c:** Differences in the different measured parameters in DRG samples from vehicle vs MC38 injected mice. *: p<0.05; **: p<0.01. **Panels d-e:** live-cell Ca-imaging on DRGs collected 3 weeks after inoculation. Number of measured cells: n= 78 and n= 138 for the vehicle and MC38 groups, respectively from at least 2 biological replicates/group. Lumbar and non-lumbar DRG neurons were cultured and tested separately for extra control (data not shown). **Panel d:** DRGs from MC38 injected mice show significantly lower resting [Ca²⁺] compared to vehicle injected mice. The columns depict the average values of the 60 sec baseline measurements for each group (***: p< 0.001). **Panel e:** Changes in intracellular [Ca²⁺] after transfusion with 25 mM KCl, for 15 sec. The first subpanel depicts the measured 340:380 ratio values throughout 60 seconds, the second depicts the peak of the KCl-induced [Ca²⁺] elevation as change in the 340:380 ratio ($\Delta F_{340:F_{380}}$). Based on the measured parameters, there is no difference in the 25 mM KCl induced Ca²⁺-response. **Panel f:** Multielectrode array of DRG cells from naïve mice with or without the addition of MC38 conditioned media (n= 8-10 wells/group, from at least 3 different cell cultures). Neuronal activity was measured every 4 hours, for 24 h. Cond. media or control solution (unconditioned MC38 media) was added after the 4 h measurement. The addition of MC38 conditioned media significantly decreases the spontaneous activity of healthy DRG cells, 16 hours after addition (*: p<0.05 vs control).

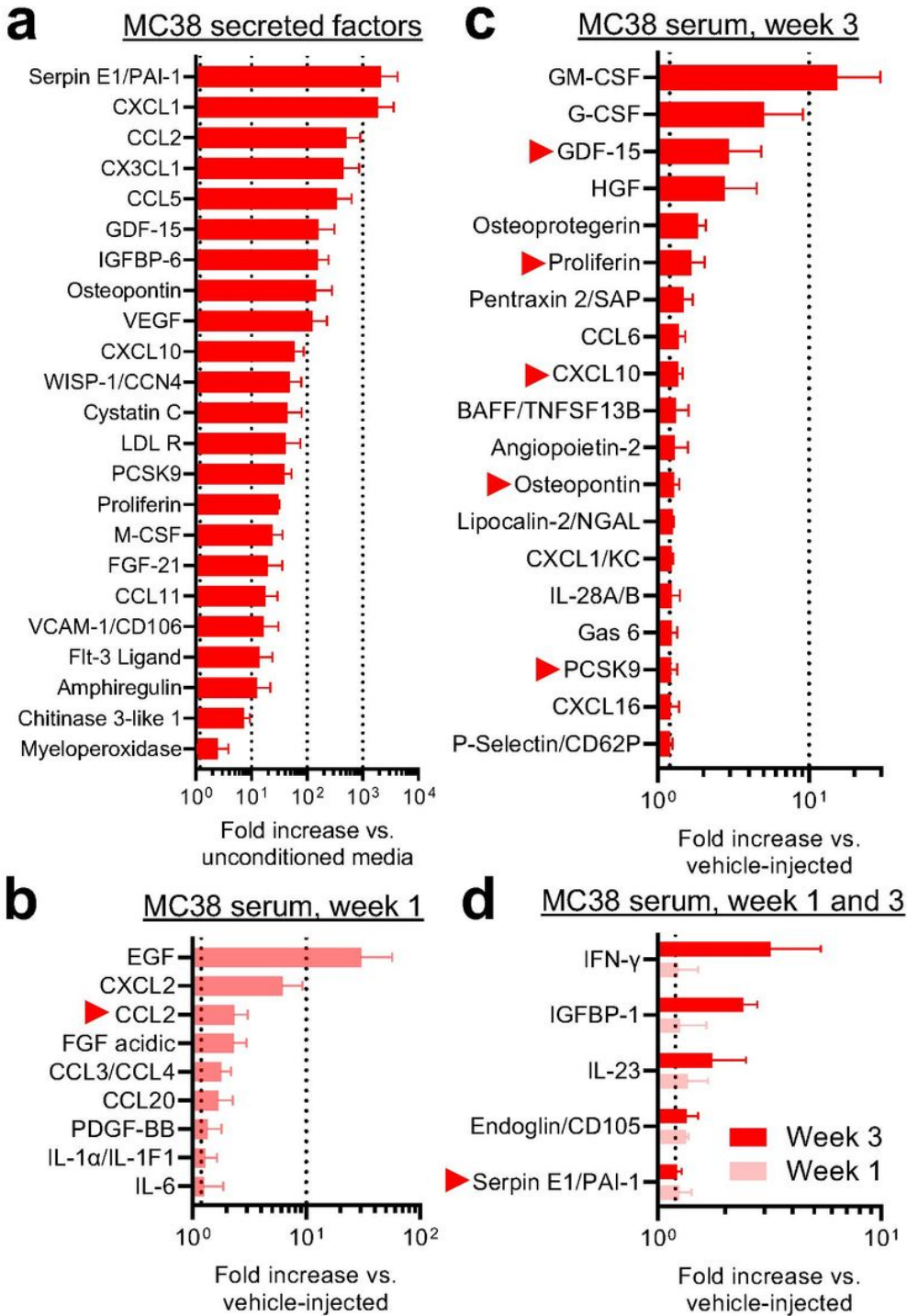


Figure 6

Factors secreted by MC38 cells and inflammatory changes in MC38 tumor-bearing mice

The change in different inflammatory mediators was measured by a complex proteome profiler array and presented as fold-change in signal intensity compared to the average of given control values (n= 3/group, in duplicates). **Panel a:** inflammatory mediators found to be secreted by MC38 cells (factors with elevated signal intensity in conditioned media vs un-conditioned media, as presented by fold-increase). **Panels b-d:** elevated inflammatory mediators in the plasma samples of MC38 injected mice compared to control (vehicle injected) mice. **Panel b:** increased factors in blood samples collected 1 week after MC38 inoculation. **Panel c:** increased

factors in blood samples collected 3 weeks after MC38 inoculation. **Panel d:** Factors increased both 1 and 3 weeks after tumor injection. Red arrows mark mediators found to be secreted by MC38 cells, as well as increased in the collected plasma samples.

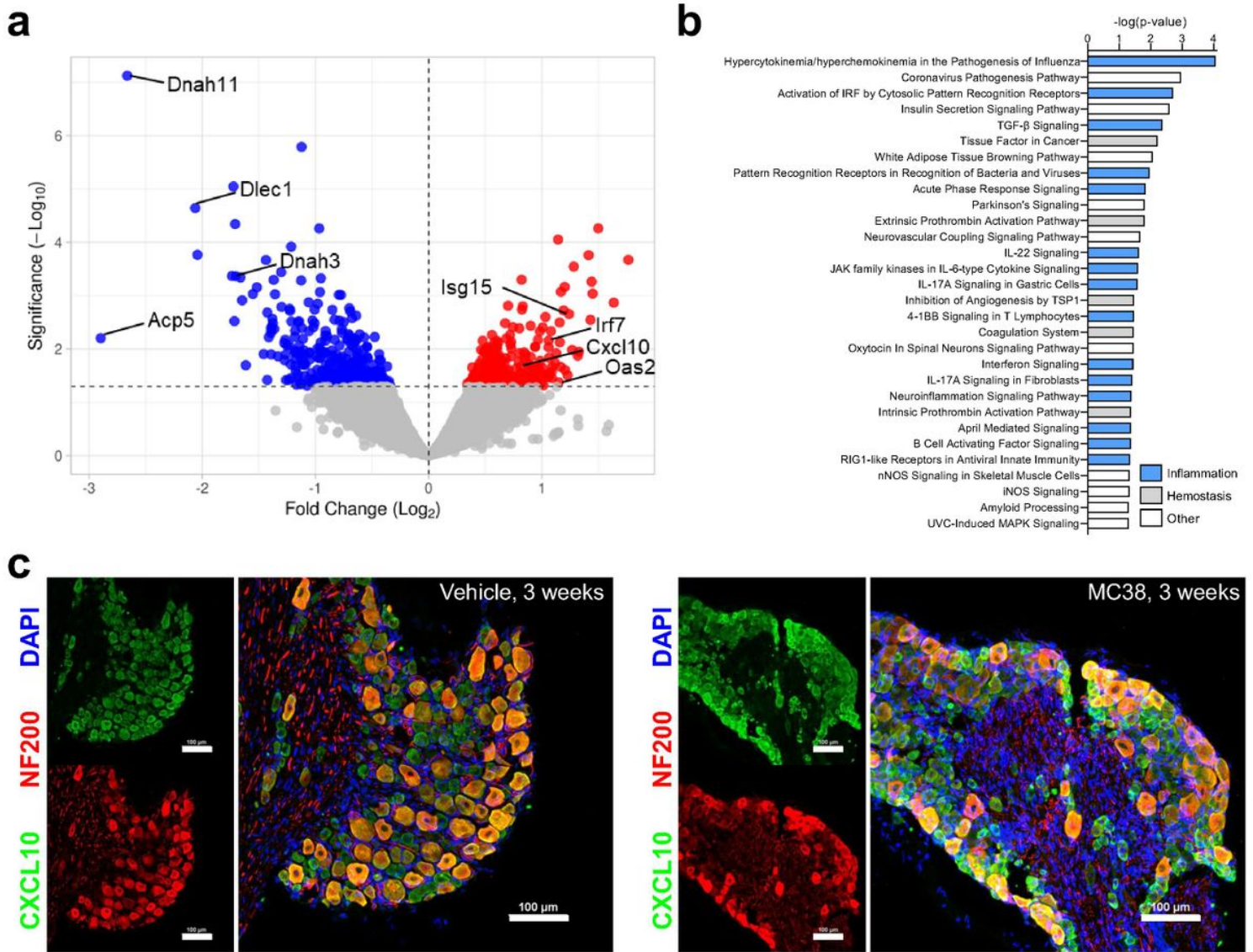


Figure 7

Bulk RNA sequencing of DRGs from MC38-injected mice

Bulk RNA sequencing analysis on lumbar DRGs of mice collected 3 weeks after tumor inoculation (n= 3/group). **Panel a:** Gene expression pathway enrichment analysis (MC38 injected vs vehicle injected mice). Blue: immune/inflammation related pathways; Grey: clotting/thrombotic pathways (consistent with the elevated levels of serpin E1, chitinase-3 like 1 in the proteome profiler arrays). **Panel b:** Volcano plot showing the different genes with significantly decreased (blue) or increased (red) expression. **Panel c:** Immunohistochemistry of lumbar DRG from vehicle-injected and MC38 tumor-bearing mice at 3 weeks indicates CXCL10 immunoreactivity (green) overlaps with the neuronal marker NF200 (red), as well as a subpopulation of small-medium diameter neurons. DAPI: blue, scale bar = 100 μm .

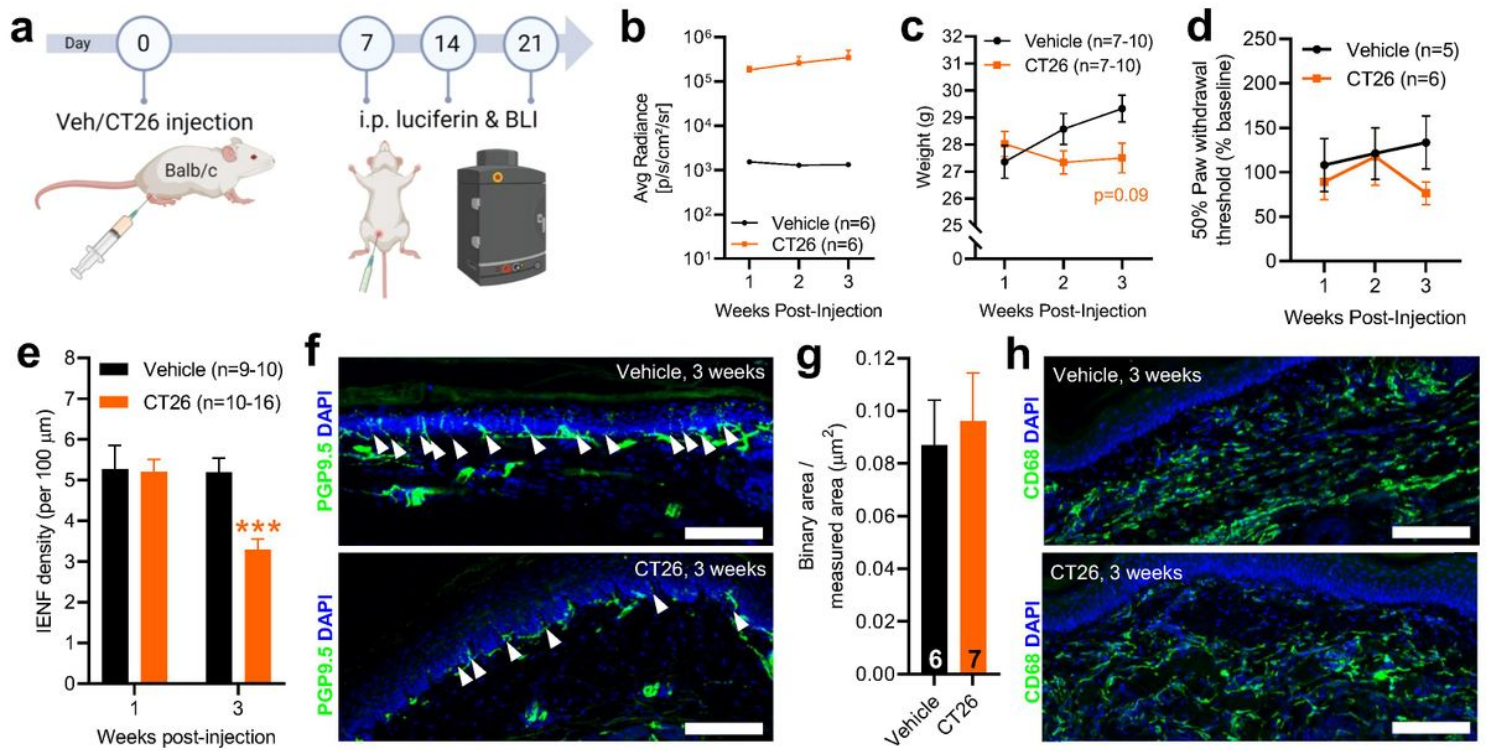


Figure 8

Tumor development, behavioral-, and IENF density changes in the CT26 colon cancer model

The data from animals with local injection of CT26 cells reveals very similar changes and patterns to the MC38 model. **Panel a:** schematic representation of the experimental protocol for the IVIS *in vivo* bioluminescence measurements (animals were measured 7, 14, and 21 days after vehicle/CT26 cell injection). The consistent robust increase in the bioluminescence signal is depicted on **panel b** and indicates persistent colon cancer development. **Panel c:** no significant change in the development (animal weight, g) of mice with or without CT26 initiated colon cancer. **Panel d:** Von Frey testing of hind paws by the up and down method revealed no significant alteration in mechanical sensitivity. Datapoints represent the average of percentage changes, compared to the measured individual baseline values (measured at week 0, before inoculation). **Panels e-h:** Immunohistochemical analysis of hind paw samples: changes in IENF (PGP9.5) and macrophage (CD68) signals. **Panel e:** changes in IENF density with time in the hind paw samples of control vs CT26 injected mice. **Panel f:** representative images show the decrease in IENF density compared to control, 3 weeks after tumor inoculation. White arrows point at the intraepidermal nerve fibers. Scale bar: 100 μm . **Panel g:** changes in CD68 signal intensity at the 3rd week in the hind paw samples of control vs CT26 injected mice. Scale bar: 100 μm . **Panel h:** representative images of hind paw samples show no change in the CD68 signal intensity of the epidermis (3 weeks after cell injection). Nuclei are stained with DAPI. Scale bar: 100 μm .

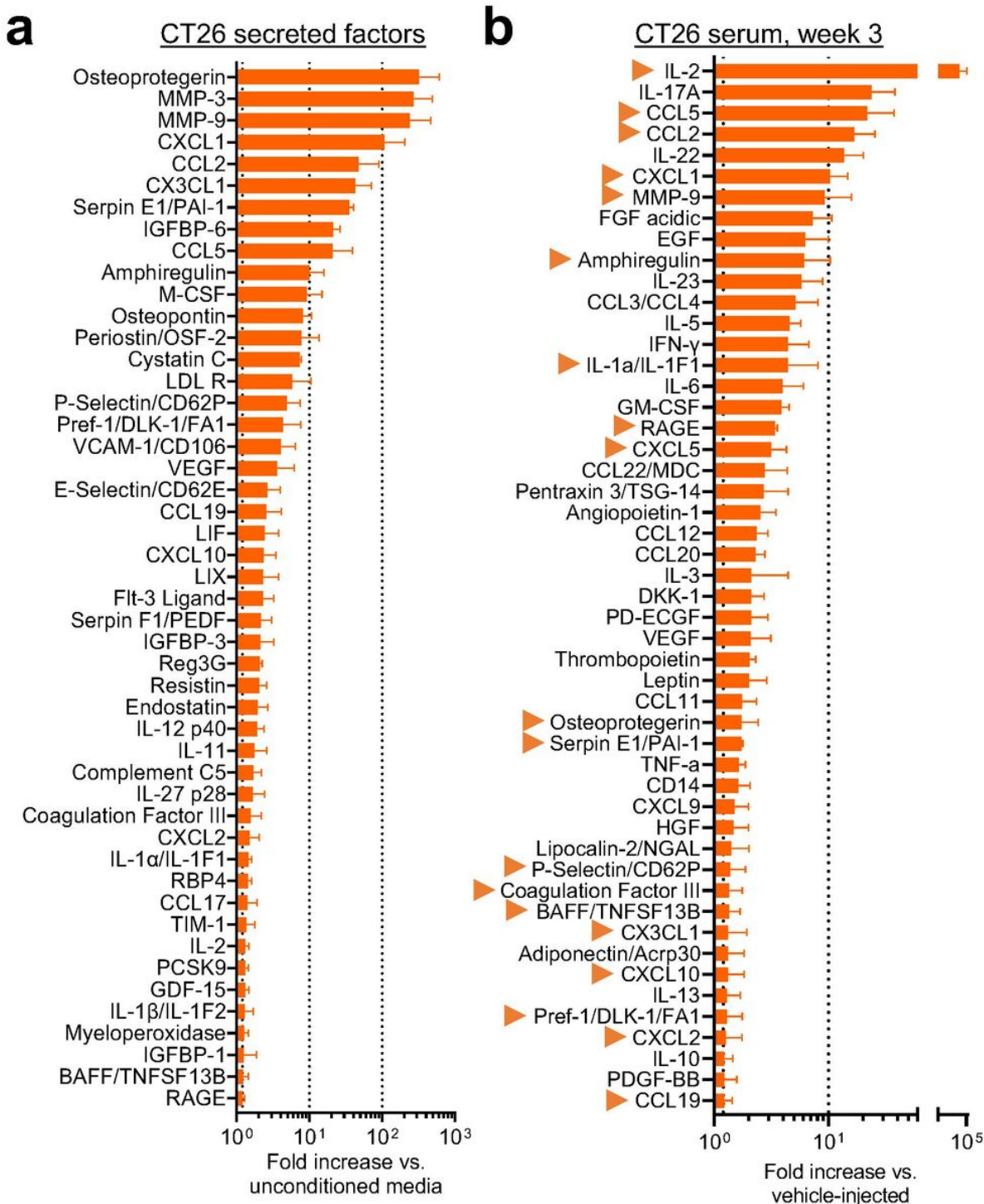


Figure 10

Factors secreted by CT26 cells and inflammatory changes in CT26 tumor-bearing mice

The change in different inflammatory mediators was measured by a complex proteome profiler array and presented as fold-change in signal intensity compared to the average of given control values (n= 3/group, in duplicates). **Panel a:** inflammatory mediators found to be secreted by CT26 cells (factors with elevated signal intensity in conditioned media vs un-conditioned media, as presented by fold-increase). **Panel b:** increased factors in blood samples collected 3 weeks after CT26 inoculation. Arrows mark mediators found to be secreted by CT26 cells, as well as increased in the collected plasma samples.

Supplementary Files

This is a list of supplementary files associated with this preprint. Click to download.

- [AdditionalTable1.docx](#)
- [AdditionalTables2and3.docx](#)
- [MC38AdditionalFigure1.pdf](#)